20. High Energy Soft QCD and Diffraction

Written February 2020 by V.A. Khoze (Durham U.; Petersburg Nuclear Phys. Inst.), M. Ryskin (Petersburg Nuclear Phys. Inst.) and M. Taševský (Prague, Inst. Phys.).

20.1 Introduction

Despite the enormous successes of Quantum Chromodynamics (QCD) (see Section 9 in [1] and [2]) there remain a number of deep questions to be answered in the domain of strong interaction physics. These concern first of all small momentum transfer processes which are generically called soft interactions.

One of the most challenging problems is the high-energy behaviour of hadronic scattering processes. At high collision energies, $\sqrt{s}$, soft interactions play a dominant role. Unfortunately, soft interactions cannot be described in terms of perturbative QCD. These are non-perturbative phenomena related to confinement which are generally considered in the context of the analytic *S*-matrix, based on *first principles*, such as analyticity, crossing symmetry and unitarity of partial waves, see e.g. [3,4]. At high energies the most self-consistent way to perform the calculations and to describe the data is the Regge approach (see for example [5–7]), which will be considered below. As discussed in Section 20.5, this formalism could be smoothly matched with perturbative QCD calculations at larger transverse momenta. Therefore, here we will concentrate on the properties of high energy soft interactions that can be expected from the extension of the perturbative QCD domain.

The main aim of this review is to present the well-established theoretical framework, based on Regge theory and QCD, used for describing high-energy collisions. A limited number of some new experimental results, mainly from the LHC, are shown in order to demonstrate that the gross features of the data are in agreement with this approach. We are not focussing on any particular phenomenological or Monte Carlo model, which are covered in the dedicated reviews and books, see e.g. Section 41 in [1], [2, 8–14] and Chapter 2 in [15].

Typically, in multiparticle production, the secondaries[1] fill the whole available rapidity interval.[2] However, there exists an important class of events in which a large interval of rapidity (typically at least 4 units) is devoid of any hadronic activity. Such an interval is called a Large Rapidity Gap (LRG). The most frequent case with a LRG is elastic scattering. There are also events in which one of the incoming protons (or both) is transformed (dissociates) into a set of two or more final state particles with the mass $M \ll \sqrt{s}$ and proton quantum number. All these events have properties similar to those of the well-known from optics pattern of diffraction of a beam of light on an obstacle. By analogy, in high-energy physics, the corresponding processes are usually called diffractive. The classic example is the elastic scattering of hadrons on nuclei (see e.g. [16]), which manifests an angular distribution with a series of minima and maxima, analogous to the diffraction of light on a black disk. At LHC energies diffractive processes constitute up to 40% of the total (pp) cross section, σ_{tot}. Therefore, we will pay special attention to the description of the elastic scattering amplitude and proton diffractive dissociation. Diffraction dissociation can be considered as a quantum mechanical process caused by the fact that different components of the incoming hadron wave function have different probabilities for interaction with a target [17]. This feature allows us to probe the transverse size of the interaction region.

Note that besides being of a fundamental interest in their own right for understanding the high energy behaviour of the QCD amplitude, there are several reasons why it is important to study

---

[1]Here and in what follows, we call secondaries the new particles produced in the course of the interaction.

[2]For definition of particle rapidity (pseudorapidity), see Section 48.5.2 in [1]; $y = \frac{1}{2} \ln \frac{E+p_z}{E-p_z}$ ($\eta = -\ln(\tan(\theta/2))$); the correct variable is the rapidity y, however, experimentally it is simpler to use the pseudorapidity η which does not require identifying the particles, setting $m = 0$. For $p_T \gg m$, $\eta \simeq y$.

soft and diffractive processes. Firstly, soft interactions unavoidably give an underlying component to rare 'hard' events, from which we hope to extract signals for New Physics. Secondly, we should be able to estimate the probability that rapidity gaps, which occur in 'hard' diffractive events, survive rescattering effects, that is, survive the population of the gaps by the secondary particles from the underlying event. Thirdly, an understanding of diffractive processes is very important for evaluation of pile-up backgrounds in high-luminosity pp collisions, which have a direct impact on various experimental measurements. Pile-up corresponds to soft independent interactions in the same bunch crossing whose number rises with increasing instantaneous luminosity. And, finally, studies of diffractive processes should help in the understanding of the structure of high-energy cosmic ray cascades, which requires a very detailed knowledge of the spectra of particles carrying a large fraction x of the incoming momentum in proton-air and nucleus-air interactions, see for instance [18].

Experimentally, diffractive processes are selected using two distinct features:

1. large regions (typically at least $\Delta\eta > 4$) in the detector are devoid of hadronic activity (LRG) and/or

2. one or both incoming particles stay intact after collision and are registered by the dedicated forward detectors placed a few hundred meters from the interaction point. The momentum loss of the initial particle, $\xi = 1 - x$, is typically smaller than 0.15.

Thus, in the case of proton-proton collisions, diffractive events correspond to elastic $pp \to pp$ scattering and to $pp \to p+X$ (Single Dissociation, SD) and $pp \to X+Y$ (Double Dissociation, DD) processes, where the $+$ sign denotes a large rapidity gap. Note that strictly speaking in high energy physics it is impossible to define (and select) rigorously purely diffractive events. We can always have some admixture of events of different origin. As a rule we call 'diffractive' the events with sufficiently large gap (with say $\Delta y > 4$, see above) and the vacuum quantum numbers transferred across the gap. Typically at the LHC the integrated cross sections of diffractive dissociation, σ_{SD}, σ_{DD}, are of the order of 5–10 mb depending on the gap size. Schematic diagrams of all discussed processes are shown in Fig. 20.1.

20.2 Regge pole approach

In pre-QCD times, in order to describe the behaviour of scattering amplitudes at high energy, $\sqrt{s}$, and small momentum-transfer squared, $-t$, Regge theory was developed and successfully applied in a wide range of energies. The Regge approach [5–7] is based on the singularities of amplitudes in the complex angular momentum, j, plane.
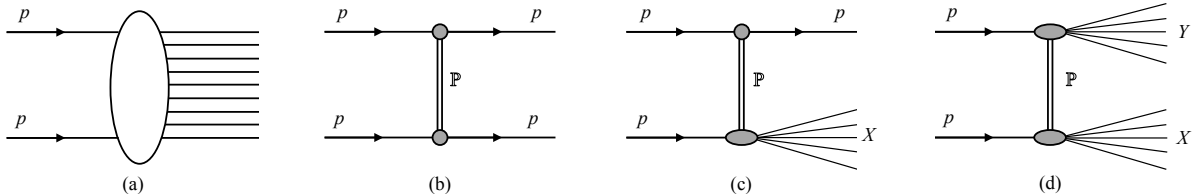

Figure 20.1: Schematic diagrams of soft pp processes. (a) non-diffractive processes, (b) elastic scattering, (c) single dissociation and (d) double dissociation. The double line corresponds to the Pomeron exchange.

For instance, the measured $\pi^- p \to \pi^0 n$ amplitude behaves as

$$T_{\pi p}(s,t) \propto s^{\alpha_\rho(t)}, \tag{20.1}$$

where the process is described by the exchange of the ρ-trajectory, $j = \alpha_\rho(t) \simeq 0.5 + 0.9t$ (with $t = (p_{\pi^-} - p_{\pi^0})^2$ in GeV^2). This trajectory passes through the spin-1 ρ-meson resonance in the 'crossed' t-channel $\pi^- \pi^0 \to \bar{p}n$; that is, $\alpha_\rho(t = m_\rho^2) = 1$. The corresponding cross section decreases with increasing s.

Figure 20.2: Illustration of the optical theorem for the total cross section and for high-mass diffractive dissociation in the absence of absorptive corrections.

On the other hand, high-energy total and elastic pp cross sections are observed to grow slowly with energy (see e.g. Section 52 in [1]) and in terms of Regge theory are dominated by the exchange of a trajectory with vacuum quantum numbers, $\sigma_{\text{tot}} \propto s^{j-1}$. The simplest possibility is to assume that the rightmost singularity in the j-plane, which drives the high-energy behaviour of the cross section, is the leading (at $t \leq 0$) Regge pole at $j = \alpha(t)$. Then the pp elastic amplitude reads

$$T_{\text{el}}(s, t) \propto s^{\alpha_\mathbb{P}(t)} . \tag{20.2}$$

The total cross section can then be conveniently expressed using the so called optical theorem which states that

$$s\sigma_{\text{tot}} = \text{Im}T_{\text{el}}(s, t = 0), \tag{20.3}$$

as illustrated in the upper part of Fig. 20.2, and thus

$$\sigma_{\text{tot}} \propto s^{\alpha_\mathbb{P}(0)-1}. \tag{20.4}$$

The pole with the largest intercept, originally assumed to be $\alpha_\mathbb{P}(0) = 1$ since high-energy total cross sections were thought to have a constant asymptotic behaviour, is called the *Pomeron*[3]

Prior to the LHC, the energy behaviour of $pp, p\bar{p}, \pi p, Kp$ cross sections was satisfactorily reproduced by the sum of the Pomeron and secondary Reggeons (the poles at lower values of j, typically with $\alpha_\rho(0) \simeq 0.5$, see [22,23] and Section 51 in [24]). However, above Tevatron energies the secondary Reggeon contributions (which all have intercepts $\alpha(0) \simeq 0.5$) are highly suppressed, which enables us to study the properties of the Pomeron only.

A popular parameterization of the elastic pp-scattering amplitude by Donnachie-Landshoff (DL) is the Regge form [25]

$$T_{\text{el}}(s, t) = \eta_P \sigma_0 F_1^2(t) s^{\alpha_\mathbb{P}(t)}, \tag{20.5}$$

---

[3]Pomeron pole was named after I. Y. Pomeranchuk. The history of the Pomeron is discussed in [19–21].

where $\sigma_0 = 21.7$ mb [26] and η_P is the signature factor

$$\eta_P = \frac{1 + \exp(-i\pi\alpha_\mathbb{P}(t))}{\sin(-\pi\alpha_\mathbb{P}(t))}, \tag{20.6}$$

F_1 is the Dirac electromagnetic form factor of the proton and the *effective* Pomeron trajectory

$$\alpha_\mathbb{P}(t) = 1 + \Delta + \alpha't \simeq 1 + 0.0808 + 0.25t, \tag{20.7}$$

with t given in GeV^2. The intercept $\alpha_\mathbb{P}(0)$ just above 1 reproduces the observed slow growth of the total hadron-hadron cross sections at high energies.

However, this simple parameterization is becoming increasingly deficient at higher energies. This is because due to unitarity we have to take into account not only Regge poles, but also the cuts in the j-plane [27, 28], which correspond to the multiple exchange of Regge poles in the t-channel, see for instance [29–31]. A powerful technique to evaluate Reggeon diagrams was developed by Gribov [7, 32] (Reggeon calculus or Reggeon Field Theory (RFT)), which allows us to calculate the multi-Pomeron contributions.

20.3 Theoretical description of high-energy diffraction

Diffractive processes (see e.g. reviews [33–37]) represent a rich testing ground for the dynamics of soft interactions as well as Monte Carlo models for soft hadron-hadron physics (see for reviews e.g. [8], Section 41 in [1] and Chapter 2 in [15]).

There is no universally agreed definition of diffractive processes. Theoretically, diffraction is the effect caused by the absorption of the incoming plane-wave in some region of impact parameter, b. After a decomposition of the distorted plane-wave over the outgoing momentum, q, due to absorption we arrive at some set of plane-waves with non-zero transverse momentum, $q_t \neq 0$. Experimentally, we call diffractive the events with large rapidity gaps (LRG) in the distribution of the final state particles. However, this definition is appropriate only for the events with very large gap sizes ($\Delta\eta > 4 - 5$); otherwise gaps can also be caused by fluctuations in the hadronization process [38].

In the case of proton-proton collisions, diffraction corresponds to elastic $pp \rightarrow pp$ scattering and to the $pp \rightarrow p + X$ and $pp \rightarrow X_1 + X_2$ processes where one or both protons are allowed to dissociate into a system X with the quantum numbers of the proton. The $p \rightarrow X$ dissociation is caused by the fact that the individual components of the incoming proton wave function interact differently with the target (see Section 20.3.1).

Theoretically, high-energy diffraction may be studied from either the s-channel or the t-channel viewpoint.

20.3.1 *Diffraction from the s-channel viewpoint*

Unitarity plays a central role in diffractive processes. To discuss unitarity effects it is convenient to work in terms of impact parameter, b. The total cross section is closely related to the elastic scattering amplitude and the scattering into inelastic final states via the s-channel unitarity of the S-matrix (see Sections 49 and 52 in [1]), $SS^\dagger = I$, or

$$disc\ T \equiv T - T^\dagger = iT^\dagger T \tag{20.8}$$

with $S = I + iT$. If we were to focus, for example, on the unitarity for elastic and quasielastic processes, then *disc T* would simply denote a cut in s-channel between incoming and outgoing particles as visualized by crosses in Fig. 20.3.

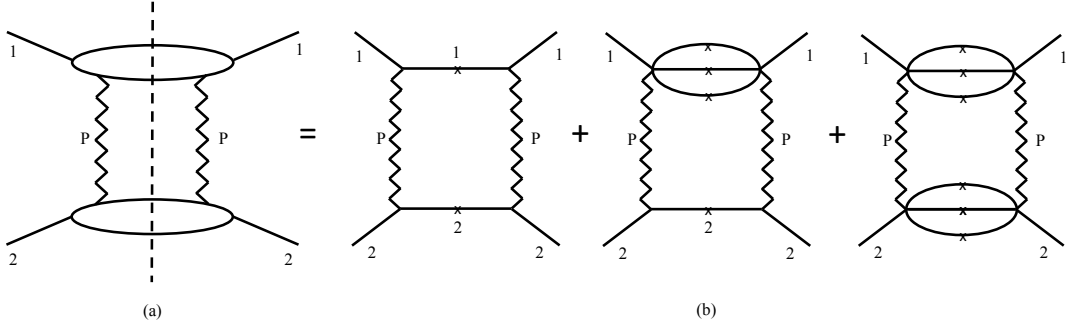At high energies, the s-channel unitarity relation is diagonal in the b basis such that

Figure 20.3: Two-Pomeron exchange in the t channel expressed as a sum over all diffractive intermediate states in the s-channel. The crosses indicate that the particles are on the mass shell.

$$2\mathrm{Im}\, T_{\mathrm{el}}(s,b) = |T_{\mathrm{el}}(s,b)|^2 + G_{\mathrm{inel}}(s,b) \tag{20.9}$$

with

$$\sigma_{\mathrm{tot}} = 2 \int d^2b \,\mathrm{Im}\, T_{\mathrm{el}}(s,b) \tag{20.10}$$

$$\sigma_{\mathrm{el}} = \int d^2b \,|T_{\mathrm{el}}(s,b)|^2 \tag{20.11}$$

$$\sigma_{\mathrm{inel}} = \int d^2b \,\Big[2\mathrm{Im}\, T_{\mathrm{el}}(s,b) - |T_{\mathrm{el}}(s,b)|^2 \Big]. \tag{20.12}$$

The general solution of Eq. (20.9) is

$$T_{\mathrm{el}}(b) = i(1 - e^{-\Omega(b)/2}) \tag{20.13}$$

and

$$G_{\mathrm{inel}}(s,b) = 1 - e^{-\mathrm{Re}\Omega(b)} = 1 - P_{\mathrm{nointer}}(s,b), \tag{20.14}$$

where G_{inel} is the sum over all inelastic intermediate states and P_{nointer} is a probability to have no inelastic interactions. $G_{\mathrm{inel}}(s,b)$ describes the b-profile of inelastic particle collisions. It satisfies the condition $0 \le G_{\mathrm{inel}} \le 1$ and determines how absorptive the interaction region is at a given impact parameter (with $G_{\mathrm{inel}} = 1$ for full absorption and $G_{\mathrm{inel}} = 0$ for the complete dominance of elastic scattering). As seen from Eq. (20.14), $\exp(-\mathrm{Re}\Omega(s,b))$ is the probability that no inelastic interactions occur at impact parameter b. Ω ($\mathrm{Re}\Omega \ge 0$) is called the opacity (optical density) or eikonal. The quantity

$$S^2(b) \equiv e^{-\mathrm{Re}\Omega(b)} = P_{\mathrm{nointer}}(b) \tag{20.15}$$

is the so-called survival factor, which enables us to calculate the probability that the LRG survives soft rescattering.

In terms of the opacity the elastic cross section takes the form

$$\frac{d\sigma_{\mathrm{el}}}{dt} = \frac{1}{16\pi s^2} |T_{\mathrm{el}}(s,t)|^2 = \frac{1}{4\pi} \left| \int d^2b \, e^{i\vec{q}_t \cdot \vec{b}}(1 - e^{-\Omega(b)/2}) \right|^2 = \pi \left| \int b\,db \, J_0(q_t b)(1 - e^{-\Omega(b)/2}) \right|^2, \tag{20.16}$$

where $q_t = \sqrt{|t|}$ and J_0 is the zeroth-order Bessel function.

To describe the elastic scattering at one fixed energy we can always find an appropriate parameterization for the opacity $\Omega(b)$ and tune the parameters to reproduce the observed $d\sigma_{el}/dt$ cross section. Moreover, we can fix the form of the parameterization, but choose, at each particular energy, the corresponding values of parameters; see, e.g. [39]. Alternatively, we may simply take the Fourier-Bessel transform from the experimental data [33, 40, 41]

$$\text{Im}T_{\text{el}}(b) \ = \ \int \frac{q_t dq_t}{4\pi} \sqrt{\frac{d\sigma_{\text{el}}}{dt} \frac{16\pi}{1+\rho^2}} \ J_0(q_t b), \tag{20.17}$$

where the square root represents $\text{Im}T_{\text{el}}(q_t)$, with $\rho \equiv \text{Re}T_{\text{el}}/\text{Im}T_{\text{el}}$. In this way, we first determine T_{el} from the data for $d\sigma_{\text{el}}/dt$, and then calculate $\Omega(b)$ using Eq. (20.13), assuming in accordance with data that ρ is small (or $\rho(t) = \text{constant}$).

At high energies $\rho^2 \ll 1$, which is usually well justified except in the diffractive dip region (see Section 20.3.3.1 for discussion of the dip region).

The value of ρ can be derived via the dispersion relation, see [3]:

$$\frac{1}{s}\text{Re}T_{\text{el}}(s) \ = \ \frac{1}{\pi} \int_{-\infty}^{+\infty} \frac{ds'}{s'-s}\sigma_{\text{tot}}(|s'|) \ = \ \frac{1}{\pi} \int_0^{\infty} \sigma_{\text{tot}}(s')\frac{2s ds'}{s'^2-s^2}. \tag{20.18}$$

Since we consider just the charge-parity C-even amplitude, here for negative s' we put $\sigma_{p\bar{p}} = \sigma_{pp}$. That is, for negative s', which corresponds to the interaction with an *anti*particle, we use the same $\sigma_{pp}(|s'|)$. The major contribution comes from $s' \simeq s$. Thus, with a good accuracy we can evaluate $\rho(t = 0)$ as

$$\rho \ \simeq \ \frac{\pi}{2} \frac{\partial \ln \sigma_{\text{tot}}(s)}{\partial \ln s}. \tag{20.19}$$

20.3.2 *Diffractive dissociation*

The elastic cross section probes the optical density of the proton. The well known example of scattering on a black disk, with $G_{\text{inel}} = 1$ for $b < R$, gives $\sigma_{\text{el}} = \sigma_{\text{inel}} = \pi R^2$ and $\sigma_{\text{tot}} = 2\pi R^2$. In general, the absorption of the initial wave (due to inelastic channels) leads, via s-channel unitarity, to elastic scattering.

Inelastic diffraction (i.e. proton dissociation) is a consequence of the *internal structure* of hadrons. This can be conveniently described at high energies, where the lifetimes of each particular Fock component of the incoming hadron/proton wave function (the hadronic fluctuations) are large, $\tau \sim E/m^2$, and during these time intervals the corresponding Fock states can be considered as 'frozen'. Each hadronic constituent can undergo a scattering with its own probability and thus destroys coherence of the fluctuations[4]. As a result, the outgoing superposition of states will be different from the incident particle, and will most likely contain multiparticle states, so we will have *inelastic*, as well as elastic scattering.

To calculate diffractive dissociation we can enlarge the set of intermediate states (p, N_a^*), from just the single elastic channel, and introduce a multichannel eikonal. However, it is more convenient to follow Good and Walker [45], and to introduce states ϕ_k diagonalising the T matrix (which e.g. in the proton case describes different $p \to N^*$, $N_a^* \to N_b^*$ transitions). Such eigenstates only undergo elastic scattering. Since there are no off-diagonal transitions,

$$\langle \phi_i | T | \phi_k \rangle = 0 \qquad \text{for } i \neq k, \tag{20.20}$$

a state k cannot diffractively dissociate into a state $j \neq k$. Working in terms of the Good-Walker eigenstates ϕ_i, we have a simple one-channel eikonal for each state. We denote the orthogonal matrix which diagonalizes T by a, so that

---

[4]At high energies the configurations with different transverse separation, r, between the quarks (valence partons) can serve as an example of such Fock states. An interaction with the QCD Pomeron does not change the value of r, while the cross section $\sigma \propto \alpha_s^2 \cdot r^2$ (see Section 20.4.2 and [42–44]).

$$T = aFa^T \qquad \text{with} \qquad \langle\phi_i|F|\phi_k\rangle = F_k\,\delta_{ik}, \tag{20.21}$$

where F_k is the probability amplitude of the hadronic process proceeding via the diffractive eigenstate ϕ_k.

Now consider the diffractive dissociation of an incoming state $|h\rangle$. We can write

$$|h\rangle = \sum_k a_{hk}\,|\phi_k\rangle. \tag{20.22}$$

The elastic scattering amplitude satisfies

$$\langle h|T|h\rangle = \sum_k |a_{hk}|^2\,F_k = \langle F\rangle, \tag{20.23}$$

where $F_k \equiv \langle\phi_k|F|\phi_k\rangle$ and where the brackets of $\langle F\rangle$ mean that we take the average of F over the initial probability distribution of diffractive eigenstates. After the diffractive scattering described by T_{fh}, the final state $|f\rangle$ will, in general, be a different superposition of eigenstates from that of $|h\rangle$, which was shown in Eq. (20.22). Neglecting the real parts, for the cross sections at a given impact parameter b, we have

$$\frac{\mathrm{d}\sigma_{\text{tot}}}{\mathrm{d}^2 b} = 2\,\mathrm{Im}\langle h|T|h\rangle = 2\sum_k |a_{hk}|^2\,\mathrm{Im}F_k = 2\langle\mathrm{Im}F\rangle$$

$$\frac{\mathrm{d}\sigma_{\text{el}}}{\mathrm{d}^2 b} = |\langle h|T|h\rangle|^2 = \left|\sum_k |a_{hk}|^2\,F_k\right|^2 = \langle|F|\rangle^2 \tag{20.24}$$

$$\frac{\mathrm{d}\sigma_{\text{el}+\text{SD}}}{\mathrm{d}^2 b} = \sum_k |\langle\phi_k|T|h\rangle|^2 = \sum_k |a_{hk}|^2\,|F_k^2| = \langle|F^2|\rangle.$$

It follows that the cross section for the single diffractive dissociation of a proton,

$$\frac{\mathrm{d}\sigma_{\text{SD}}}{\mathrm{d}^2 b} = \langle|F^2|\rangle - \langle|F|\rangle^2, \tag{20.25}$$

is given by the statistical dispersion in the absorption probabilities of the diffractive eigenstates. Here the average is taken over the components k of the incoming proton which dissociates. If the averages are taken over the components of both of the incoming particles, then Eq. (20.25) is the sum of the cross sections for single and double dissociation, see Fig. 20.3.

Note that if all the components ϕ_k of the incoming proton $|h\rangle$ were absorbed equally, then the diffracted superposition would be proportional to the incident one and the probability of the inelastic diffraction would be zero. Thus if, at very high energies, the amplitudes F_k at small impact parameters are equal to the black disk limit, $F_k = i$, then diffractive production will be equal to zero in this impact parameter domain, and so will only occur in the peripheral b region where the edge of the disk becomes not completely black. Hence the impact parameter structure of diffractive dissociation and elastic scattering is drastically different in the presence of absorptive s-channel unitarity effects (see the G_{inel} term in Eq. (20.9)). Under the assumption that amplitudes F_k at high energies cannot exceed the black disk limit, $\mathrm{Im}\,F_k \leq 1$, equations 20.24 lead to the following bound

$$\frac{\mathrm{d}\sigma_{\text{el}+\text{SD}_1+\text{SD}_2+\text{DD}}}{\mathrm{d}^2 b} \leq \frac{1}{2}\frac{\mathrm{d}\sigma_{\text{tot}}}{\mathrm{d}^2 b}. \tag{20.26}$$

known as the Pumplin bound [46] [5].

---

[5]Strictly speaking the proof of the Pumplin bound is justified only for low mass dissociation. When the masses $M_{1,2}$ become so large (say, $M_i^2 > \sqrt{ss_0}$) that the Good-Walker states $|\phi_i\rangle$, corresponding to two incoming protons overlap, we may face double counting. Therefore, the high mass dissociation will be considered in the next Section, in terms of the multi-Pomeron diagram. Here and in what follows s_0 is a constant which should be defined for a particular theoretical model or fitted from experiment.

20.3.3 *Diffraction from the t-channel viewpoint*

The *t*-channel approach is based on the Regge model (see Section 20.2), where high-energy diffractive processes are mediated by the exchange of a Pomeron ($\mathbb{P}$). In the case of the elastic *pp*-scattering amplitude in the eikonal model (see Eq. (20.13)), the opacity corresponding to the exchange of one Pomeron is

$$\Omega(s,b) = \int \frac{\mathrm{d}^2 q_t}{4\pi^2} \ \Omega(s,q_t) \ e^{i\vec{q_t}\cdot\vec{b}} \tag{20.27}$$

with

$$\Omega(s,q_t) = \frac{1}{s}T'_{\mathrm{el}} = -i\eta_P(t)g_N(t)g_N(t)\left(\frac{s}{s_0}\right)^{\alpha_{\mathbb{P}}(t)-1}, \tag{20.28}$$

where T'_{el} is the two-particle s-channel irreducible elastic amplitude, cf. Eq. (20.5), and $g_N(t)$ is the proton-Pomeron coupling.

If we assume an exponential *t*-dependence of the coupling, $g_N(t) = g_N(0)\exp(B_0 t)$, and neglect the Pomeron phase, then the opacity is

$$\Omega(s,q_t) = g_N(0)g_N(0)\left(\frac{s}{s_0}\right)^{\alpha_{\mathbb{P}}(0)-1}e^{Bt}, \tag{20.29}$$

with the *t*-slope given by

$$B \ = \ 2B_0 + \alpha'_{\mathbb{P}}\ln\left(\frac{s}{s_0}\right). \tag{20.30}$$

At high energies the opacity has a Gaussian form in the *b*-space:

$$\Omega(s,b) = \frac{g_N^2(0)}{4\pi B}\left(\frac{s}{s_0}\right)^{\alpha_{\mathbb{P}}(0)-1}e^{-b^2/4B}. \tag{20.31}$$

In terms of opacity the effective radius of interaction increases at high energies as $\sqrt{\alpha'_{\mathbb{P}}\ln(s/s_0)}$. This means that with energy increasing the differential cross section becomes steeper (the so called *shrinkage* of the diffractive peak).

If we were to take for the Pomeron the DL parametrisation [25,26], that is to keep just the first, $T(b) = \Omega(b)/2$, term in the elastic amplitude (Eq. (20.13)) then, at LHC energies, the Gaussian would exceed the black disk limit at small *b*. However, the eikonal unitarization reduces the power growth of the one-Pomeron exchange cross section. Thus, in Eq. (20.31) $\Omega(s,b) \propto (s/s_0)^{\alpha_{\mathbb{P}}-1}$ gives an amplitude $\mathrm{Im}\,T_{\mathrm{el}}(s,b) = 1 - e^{-\Omega/2} < 1$. Hence the total cross section is limited by the size of the effective interaction area $\sigma_{\mathrm{tot}} < 2\pi R^2$, where the interaction radius R can be estimated from Eq. (20.31) as the value of *b* where $\mathrm{Re}\,\Omega(b)$ becomes ~ 1.

For the parameterization of Eq. (20.31) the corresponding radius grows at very large energies as

$$b^2 = R^2 = 4B\ln\left[\frac{g_N^2(0)}{4\pi B}\left(\frac{s}{s_0}\right)^{\alpha_{\mathbb{P}}(0)-1}\right] \simeq 4\Delta\alpha'_{\mathbb{P}}\ln^2(s/s_0). \tag{20.32}$$

That is for $\Delta = 0.1$ and $\alpha'_{\mathbb{P}}=0.25$ GeV^{-2} we may expect that the cross section increases as

$$\sigma_{\mathrm{tot}} = 2\pi R^2 \simeq c\cdot\ln^2 s, \tag{20.33}$$

with $c = 8\pi\Delta\alpha'_{\mathbb{P}} = 0.24$ mb. This value is close to that obtained by the COMPETE parameterization ($c = 0.27$ mb [22,24]) but much smaller than the Froissart-Lukaszuk-Martin (FLM) bound [47–49]. With $c^{\mathrm{FLM}} = \pi/m_\pi^2 \simeq 60$ mb, see Section 20.7,

$$\sigma_{\mathrm{tot}} \leq \frac{\pi}{m_\pi^2}\ln^2\left(\frac{s}{s_0}\right). \tag{20.34}$$

The fact that $c = (0.24\text{--}0.27)$ mb $\ll c^{\text{FLM}} = 60$ mb demonstrates that even at the LHC we are very far from true high-energy asymptotics [6], and the observed growth of the cross section is driven by the interactions at relatively large transverse momenta $k_t \gg m_\pi$ rather than the smallest hadron mass m_π in the denominator of Eq. (20.34).

20.3.3.1 *The t-slope and dip in the elastic cross section*

We first start with a relatively small one-Pomeron amplitude and consider the two-Pomeron contribution corresponding to the Ω^2 term in the expansion of the eikonal $1 - \exp(-\Omega/2)$. In this term the momentum transferred, $q_t = \sqrt{|t|}$, is divided between the two Pomerons so that each Pomeron carries about a momentum $q_t/2$. Correspondingly, the t dependence of the whole 'two-Pomeron' amplitude will be $\exp(2B(t/4)) = \exp(Bt/2)$ [7].

Since the two-Pomeron contribution has an opposite sign in comparison with the one-Pomeron exchange, their interference will result in the appearance of the first diffractive minimum which moves to smaller $|t|$ with energy increasing. Such interference effects are largely responsible for the zero in the imaginary part of the amplitude (with the minimum filled by the real part).

It is worth mentioning that the one-channel eikonal discussed so far is a rather oversimplified approximation. It provides some indications about the behaviour we may expect for the elastic cross section, but clearly it does not give the whole story. Moreover, even within the framework of the one-channel eikonal, the expectation for the elastic slope t-dependence could be masked by other effects. Firstly, there is no reason why the t-dependence of the proton-Pomeron coupling $g_N(t)$ has to be a pure exponent. Next, there exists a two-pion singularity at $t = 4m_\pi^2$ (close to the physical region) in the Pomeron trajectory which generates some curvature in the behaviour of $\mathrm{d}\sigma_{\text{el}}/\mathrm{d}t$ [50–52]. So there may be some compensation between the effects caused by the eikonal (arising from the interference between the different multi-Pomeron contributions), and the curvatures coming from the form of the proton-Pomeron coupling and the two-pion singularity of the Pomeron trajectory. However, an exact compensation looks quite non-trivial and a *pure* exponential behaviour of $\mathrm{d}\sigma_{\text{el}}/\mathrm{d}t$ looks highly unlikely.

Indeed, the measurements by the TOTEM collaboration at 8 TeV [53] and at 13 TeV [54] clearly demonstrate that the local slope of the elastic pp cross section,

$$B = \mathrm{d}[\ln(\mathrm{d}\sigma_{\text{el}}/\mathrm{d}t)]/\mathrm{d}t, \tag{20.35}$$

at $-t \lesssim 0.3$ GeV^2 varies with t.

20.3.3.2 *High mass dissociation*

Let us turn to inelastic diffractive processes that is, to single and double proton dissociations, $pp \rightarrow X + p$ and $pp \rightarrow X_1 + X_2$, where the + sign denotes the presence of a LRG in the distribution of final state particles. For example, for the diffractive dissociation of a proton into a system of mass M, the rapidity gap between the incoming proton and the remaining hadrons is

$$\Delta y = \ln\left(\frac{s}{M^2}\right) = \ln\left(\frac{1}{\xi}\right), \tag{20.36}$$

where $\xi = 1 - x$ and x is the initial momentum fraction (Feynman variable) carried by the outgoing proton. The masses, M, of the diffractively excited states, produced in high $\sqrt{s}$ collisions, can be large. To separate dissociation from the common inelastic process, usually the condition $M^2 \ll s$ is imposed.

The simplest multi-Pomeron diagram used to describe the diffractive dissociation is the so-called triple-Pomeron graph, shown at the end of Fig. 20.2.

---

[6]As usual, we assume $s_0 = 1$ GeV^2, but the qualitative conclusion does not depend on any realistic choice of s_0.

[7]The two-Pomeron contribution has a factor of two smaller t-slope, and in terms of the impact parameter, the $\Omega^2(b)$ term is concentrated in the domain of a smaller radius. In such a simplified picture, the impact parameters corresponding to an exchange of n Pomerons will rapidly decrease with n increasing.

In the Regge pole model, the cross section for the inclusive single diffractive (SD) dissociation process [55–57] can be written in the form (see Fig. 20.2)

$$\frac{\xi \mathrm{d}\sigma_{\mathrm{SD}}}{\mathrm{d}t\mathrm{d}\xi} = \frac{M^2 \mathrm{d}\sigma_{\mathrm{SD}}}{\mathrm{d}t\mathrm{d}M^2} = \frac{g_{3\mathbb{P}}(t)g_N(0)g_N^2(t)}{16\pi^2} \left(\frac{s}{M^2}\right)^{2\alpha_{\mathbb{P}}(t)-2} \left(\frac{M^2}{s_0}\right)^{\alpha_{\mathbb{P}}(0)-1}, \qquad (20.37)$$

where $g_{3\mathbb{P}}(t)$ is the triple-Pomeron coupling. The value of the coupling $g_{3\mathbb{P}}$ is usually obtained from a triple-Regge analysis of lower energy data (see e.g. [34]) .

In an analogous way the cross section for double dissociation reads

$$\frac{\xi_1\xi_2 \mathrm{d}\sigma_{\mathrm{DD}}}{\mathrm{d}t\mathrm{d}\xi_1\xi_2} = \frac{M_1^2 M_2^2 \mathrm{d}\sigma_{\mathrm{DD}}}{\mathrm{d}t\mathrm{d}M_1^2\mathrm{d}M_2^2} = \frac{g_{3\mathbb{P}}^2(t)g_N^2(0)}{16\pi^3} \left(\frac{ss_0}{M_1^2 M_2^2}\right)^{2\alpha_{\mathbb{P}}(t)-2} \left(\frac{M_1^2 M_2^2}{s_0^2}\right)^{\alpha_{\mathbb{P}}(0)-1}, \qquad (20.38)$$

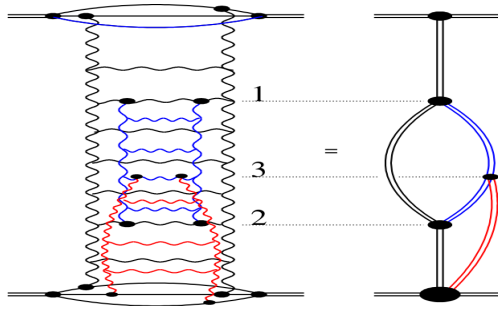where t is the momentum squared transferred through the LRG. As discussed in Section 20.5, from

Figure 20.4: Pomeron exchange with schematic diagrams for the enhanced and semi-enhanced exchanges.

a microscopic point of view the Pomeron exchange is described by a set of ladder-type diagrams (see [58–60]), which can lead to a rescattering of the intermediate partons (produced inside this ladder during the evolution), see Fig. 20.4. The left plot shows the Pomeron exchange complemented with the rescattering of partons 1 and 2 and the scattering of a parton 3 on the target. In terms of multi-Pomeron exchanges this corresponds to the diagram on the right hand side, where the Pomeron exchange is shown by the double line of a corresponding colour. The blue one is called "enhanced" (its contribution is integrated over the rapidities of both upper and lower vertices, i.e. of partons 1 and 2). The loop formed by the Pomerons shown in red is called "semi-enhanced" (it is integrated over the rapidity of one intermediate parton).

While the rescattering of the incoming hadron (proton) is already embedded in the eikonal formula (Eq. (20.13)), the rescattering of the intermediate partons in RFT is accounted for by the so-called enhanced diagrams [8] with multi-Pomeron vertices, g_m^n, which couple m to n Pomerons. It is quite a challenging task to resum all the enhanced diagrams, however this was successfully performed within the framework of the QGSJET Monte Carlo [61]. An elegant approach to sum up all enhanced diagrams in the case when each extra effective Pomeron contribution is very large was proposed in [62], assuming the analyticity of the g_m^n vertices in n and m in the right half of the complex n- and m-planes. The resulting amplitude becomes a black disk.

The simplest triple-Pomeron vertex $g_2^1 = g_{3\mathbb{P}}$ produces the first multi-Pomeron graph considered above (see the end of Fig. 20.2). However, numerically the multi-Pomeron vertices are relatively

---

[8]This contribution is *enhanced* due to the large parton multiplicity.

small. Note also that the value of $g_{3\mathbb{P}}$, determined from the fit to experimental data (e.g. [63]), is actually an effective vertex with coupling

$$g_{\mathrm{eff}} \ = \ g_{3\mathbb{P}} \, \langle S^2 \rangle, \tag{20.39}$$

which already includes the survival factor $S^2(b)$, see Eq. (20.15).

Since the opacity Ω increases with energy, at large Ω the number of multiple interactions grows as $N \propto \Omega$, leading to a smaller S^2. An explicit analysis [64] accounting for the survival effects gives a coupling $g_{3\mathbb{P}}$ about a factor of 3 larger than g_{eff}, namely $g_{3\mathbb{P}} \simeq 0.2 g_N$.

Recall that the Pomeron exchange simultaneously describes both the elastic scattering amplitude, T_{el}, and the multiparticle production cross section, G_{inel}. The discontinuity (*disc* T_{el}) of the ladder diagram corresponds to the production of secondary particles, practically homogeneously distributed over the whole available rapidity interval covered by the Pomeron, as illustrated by the right-hand diagram in Fig. 20.5.
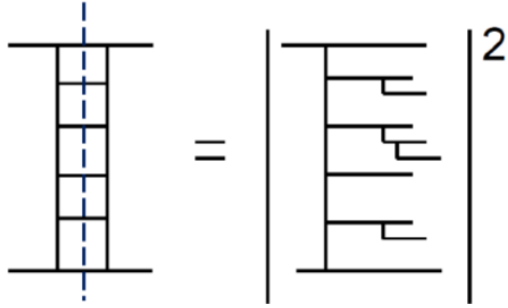

Figure 20.5: Cut Pomeron contribution to the inelastic cross section.

For the one-Pomeron case this discontinuity is called the "cut Pomeron". Correspondingly each multi-Pomeron diagram describes a series of different processes. Cutting k Pomerons in the diagram with n Pomerons we get the inelastic interaction with the multiplicity (density of secondaries) k times larger than that, N_0, produced by one cut Pomeron, $dN/dy = k \cdot N_0$. The remaining $n - k$ (elastic) Pomerons account for the absorptive corrections to the subprocess with k cut Pomerons. Indeed, the contribution of the diagram with n Pomerons includes also the processes with larger, $(k+i) \cdot N_0$ multiplicities (cut Pomerons), where $(i = 1, 2, ..., n-k)$. Absorptive corrections, described by the remaining elastic Pomerons, play a role of the survival factor S^2 for the process with the fixed particle density $k \cdot N_0$. They ensure probability conservation (the sum of the probabilities of all possible different channels is equal to one) and restore unitarity. Note that the multi-Pomeron diagrams represent all possible interactions between partons from the protons and partons from the Pomerons. In the case of Monte Carlo generators, the non-enhanced multi-Pomeron contributions are included in terms of the multiple parton interaction (MPI) option, see [13,65] and Section 7.2 in [2]. However, as a rule, this option accounts mainly for the multiple interactions between the partons from the protons (incoming hadrons). The energy-momentum sharing between the various inelastic rescattering processes (including the cut and uncut Pomerons) was performed at the amplitude level within the EPOS Monte Carlo [66].

20.3.3.3 *AGK cutting rules*

The relation between the cross sections of subprocesses with a different number of cut Pomerons within a given diagram with n Pomerons) is given by the AGK (Abramovsky-Gribov-Kancheli [67]) cutting rules. These rules include also the cut *between* the Pomerons with $k = 0$ which corresponds to the contribution of the particular diagram to the elastic cross section. By applying these rules,

it is possible to show the self-consistency of the approach, which was lacking in the pure Regge-pole model.

Consider a diagram where the elastic scattering amplitude is mediated by an exchange of n Pomerons. The AGK cutting rules specify the coefficients c_n^k arising when k of these Pomerons are cut. Recall that the Pomeron cut discontinuities give the corresponding inelastic contributions to σ_{tot}. The terms with $k = 0$ correspond to the diffractive cutting of the diagram (that is, the cut is between the Pomeron exchanges, and not through the Pomerons themselves), while the terms with $k = 1, 2, ...$ describe the processes with k cut Pomerons. The coefficients $c_n^k = \sigma_n^k / |\sigma_{\text{tot}}^{(n)}|$ are [9]

$$c_n^{k=0} = (-1)^n (2^{n-1} - 1), \qquad c_n^{k \neq 0} = (-2)^{n-1} \frac{(-1)^{k-1} n!}{k!(n-k)!} \qquad (20.40)$$

where $\sigma_{\text{tot}}^{(n)}$ denotes the contribution of the n-Pomeron diagram to the total cross section. Note the alternating sign of $\sigma_{\text{tot}}^{(n)}$ expressed as $(-1)^{n-1}$.
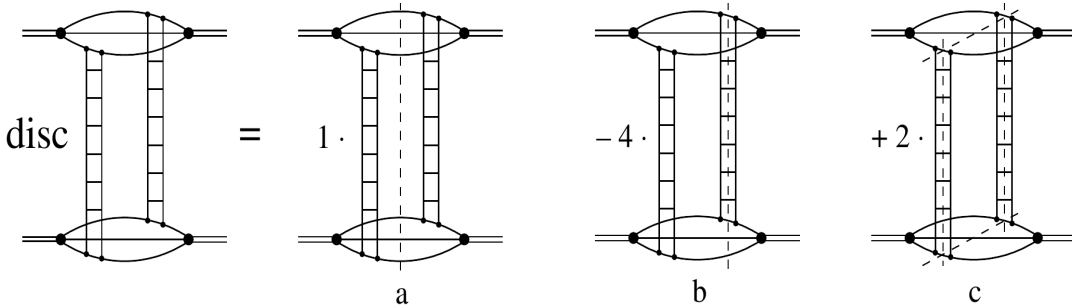

Figure 20.6: Two-Pomeron exchange diagram as a sum of different AGK cuts shown by the dashed lines.

For the two-Pomeron exchange, $n = 2$, the coefficients are $+1$, -4, or $+2$ according to whether $k = 0$, 1 or 2 Pomerons are cut, respectively. As shown in Fig. 20.6, the amplitude of the two-Pomeron exchange corresponds to a sum of three processes: i) inelastic interaction with particle density twice that caused by one Pomeron (see Fig. 20.6(c)) which enters with the coefficient '2', ii) shadowing (absorptive) correction to the one-Pomeron exchange contribution, which corresponds to events with a single Pomeron density (only one Pomeron is cut), see Fig. 20.6 (b), which enters with a factor '-4', and iii) diffractive elastic scattering or proton dissociation (when different components of the proton wave function correspond to different interaction cross sections), caused by the distortion of the incoming plane wave, see Fig. 20.6(a).

Note that the inclusive cross section is not affected by the multi-Pomeron contribution: $2 \times (2) + 1 \times (-4) = 0$. This is a general property of the AGK rules valid for any number of Pomerons n. Thus in order to calculate the inclusive single-particle cross section, it is sufficient to consider just the *one*-Pomeron exchange diagram.

Let us emphasize that the AGK rules provide a framework to consistently work with multi-Pomeron diagrams, that is, with the Regge cuts, accounting for their contributions to different processes (elastic scattering and diffractive dissociation, inelastic events with different densities, dN/dy, of secondaries, etc.).

Measurements of diffractive dissociation cross sections have been made in a wide range of pre-LHC energies, see e.g. [68–73]. At the LHC, cross sections of events with a LRG were measured by the ATLAS, CMS and ALICE collaborations at 7 and 8 TeV, see [74–77]. ATLAS [78] and

---

[9] In their complete form the AGK cutting rules were implemented in the QGSJET Monte Carlo [61].

CMS and TOTEM [79] presented first measurements of SD cross sections at 8 TeV with a tagged forward proton. While ATLAS measured inclusive SD cross section, CMS and TOTEM studied SD dijet production. Note that in [78] the measured slope $B = 7.65 \pm 0.34$ GeV^{-2} of the inclusive SD cross section as well as the differential distributions $\frac{\xi \mathrm{d}\sigma_{\mathrm{SD}}}{\mathrm{d}t\mathrm{d}\xi}$ for $0.0001 \leq \xi \leq 0.025$ are (within the experimental uncertainties) in a good agreement with the theoretical expectations [29, 80]. Moreover a relatively small (in comparison with the $\mathrm{d}\sigma_{\mathrm{el}}/\mathrm{d}t$) slope B indicates that the size of the triple-Pomeron vertex is much smaller than the proton size.

20.3.4 *Central Diffractive processes*

Processes $pp \rightarrow p+X+p$, where an object X, produced in the central rapidity region, is separated from the outgoing protons by a LRG on each side, are called Central Exclusive Production (CEP). They are described by the double Pomeron exchange (DPE) diagrams. When the mass of the central system, M_X, is large and the interaction in the M_X region can be described by Pomeron exchange, the corresponding cross section reads

$$\frac{\xi_1\xi_2\mathrm{d}\sigma^{\mathrm{CEP}}}{\mathrm{d}\xi_1\mathrm{d}t_1\mathrm{d}\xi_2\mathrm{d}t_2} = \frac{g_N^2(t_1)g_N^2(t_2)}{(16\pi^2)^2}\left(\frac{1}{\xi_1}\right)^{2\alpha_{\mathbb{P}}(t_1)-2}\left(\frac{1}{\xi_2}\right)^{2\alpha_{\mathbb{P}}(t_2)-2} g_{3\mathbb{P}}^2(0)\left(\frac{M_X^2}{s_0}\right)^{\alpha_{\mathbb{P}}(0)-1} . \quad (20.41)$$

If the mass M_X is not too large or for the cases (such as exclusive Higgs boson or dijet production) where the mass M_X is comparable with the corresponding hard scale, the last factor $g_{3\mathbb{P}}^2(0)(M_X^2/s_0)^{\alpha_{\mathbb{P}}(0)-1}$ should be replaced by the corresponding 'Pomeron-Pomeron cross section', see for instance [81, 82].

Note that equations (20.37), (20.38) and (20.41) are written in a simplified way without accounting for absorptive corrections. That is, the cross sections in equations (20.37) (20.38) and (20.41) should be multiplied by the gap survival factor S^2 (see Eq. (20.15)).

Since the QCD Pomeron is built mainly from gluons it is natural to search for glueballs in double Pomeron exchange processes, and in particular, in CEP.

Resonance production in the Pomeron-Pomeron fusion was extensively studied at the CERN ISR at $\sqrt{s}$ from 22 GeV to 63 GeV (see for reviews [82–84]) and, after the ISR closure in 1983, in fixed target experiments at the CERN SPS [85] and E690 at the Tevatron [86, 87]. Glueballs were actively searched for and the properties of the f_0 and f_2 production studied in detail using multiparticle spectrometers, such as the Omega facility at the CERN SPS experiments (WA76, WA91 and WA102), see for a review [85].

An important property of CEP processes, which can be expected from matching with the perturbative QCD LO (leading order) calculation, is the $J_z = 0$ dominance. Perturbatively, for the CEP of a heavy object, the leading contribution comes from a configuration with the projection of this object spin onto the beam axis $J_z = 0$ [81]. Note that the CEP cross section is suppressed at large M_X by a strong bremsstrahlung off the incoming gluons (from the Pomeron) which would violate the 'exclusivity'. The small probability of not having such radiation is described by the Sudakov suppression factor, T_{Sud}, [88], see [81] for details.

20.3.5 *Diffractive parton distributions*

Selecting in Deep Inelastic Scattering (DIS) events with a LRG (see e.g. [89, 90]) or detecting the leading proton (see Section V.C. in the review [91]) we can study the parton (quark and gluon) distributions of the Pomeron [10]. In other words, such events can be treated as DIS on the Pomeron target with the incoming Pomeron flux given by

$$f_{\mathbb{P}}(x_{\mathbb{P}}) = \int \mathrm{d}t \frac{g_N^2(t)}{16\pi^2} x_{\mathbb{P}}^{2(1-\alpha_{\mathbb{P}}(t))} , \quad (20.42)$$

---

[10]see also Section 18.5 in [1]

where the proton momentum fraction transferred through the Pomeron $x_{\mathbb{P}} = \xi = M^2/s$.

These Pomeron PDFs were extracted from the HERA measurements of ep scattering with leading protons or a LRG and can be used to describe the inclusive production of high E_T dijets or another hard process based on the collinear factorization theorem in the same way as that in non-diffractive collisions (see [91]). The inclusive measurements of these PDFs are described in [92–94], with the combined H1 and ZEUS data using tagged protons analyzed in [95]. The impact of diffractive jet measurements is addressed e.g. in [96] and the measured charm contribution is presented in [97, 98]. As far as the parton distributions are known, we can calculate the corresponding inelastic cross section of the Pomeron-proton interaction using one of the 'general purpose' Monte Carlo generators (see e.g. [13]), multiply it by the Pomeron flux and compare the obtained result with the Regge formula in Eq. (20.37). This approach provides another way to evaluate the triple-Pomeron vertex $g_{3\mathbb{P}}$. The corresponding analysis was performed in [99] and leads to practically the same (within the error bars) value of $g_{3\mathbb{P}} = 0.2g_N(0)$.

It is worth mentioning that in DIS at large Q^2 we are dealing with small-size objects and the rescattering effects are small. Therefore, the survival factor $S^2 \simeq 1$ and does not affect the results.

20.4 Experimental data on diffraction at high energies

20.4.1 *Total and elastic cross sections*

The elastic scattering of protons is a process with a special and rather simple experimental signature: the central detector is empty while the incoming protons after the collisions are detected in the dedicated forward proton detectors (FPD) placed far from the interaction point (IP). Elastic scattering data are taken in special runs in order to be able to reach different ranges of t-values and thanks to the very large value of the cross section the data can be collected with a relatively low instantaneous luminosity and hence a negligible pile-up.[11]

These special runs usually have very few proton bunches and differ in the t range covered, which is governed roughly by the relation $t_{\min} \propto d^2/\beta^*$. Here d is the distance, expressed in multiples of the beam size at the detector, from the centre of the LHC beam and β^* is defined as the distance from the IP to the point where the transverse area of the beam is twice as wide as that at the IP (see Section 31 in [1]). Note that if we work at large β^*, the incoming protons have very small angular divergence leading to small average transverse momentum, which allows us to measure very small $|t|$ values. The lowest $|t|$ values measured so far at the LHC are 4×10^{-4} GeV^2 (ALFA) and 6×10^{-4} GeV^2 (TOTEM) reached with the 8 TeV LHC beam configured with β^*=1 km optics. The largest t values of about 4 GeV^2 were measured by TOTEM at 8 and 13 TeV with $\beta^* = 90$ m thanks to special triggers. Other β^* values used in special runs are 3.5 m, 11 m and 2.5 km.

There are four ways to determine the σ_{tot} value:

1. **Elastic and Inelastic.** This method does not require the optical theorem and hence no extrapolation of $d\sigma_{\text{el}}/dt$ to $t = 0$ and no ρ (defined below Eq. (20.17)) but rather the luminosity and measuring rates N_{el} (elastic) and N_{inel} (inelastic). The total cross section is then simply:

$$\sigma_{\text{tot}} = \frac{1}{\mathcal{L}}(N_{\text{el}} + N_{\text{inel}}). \tag{20.43}$$

Of course, both N_{el} and N_{inel} should be corrected for the detector acceptance and efficiency. This is especially important for N_{inel} since the detectors never cover the whole rapidity region (i.e. the whole 4π).

2. **Elastic only.** This approach necessitates measuring $d\sigma_{\text{el}}/dt$ and using the optical theorem with a known value of ρ. As explained in Section 20.2, the optical theorem states that

---

[11]The pile-up is formed by additional pp collisions which typically produce low-p_T particles. These may affect the signal sample and worsen various reconstruction and identification efficiencies.
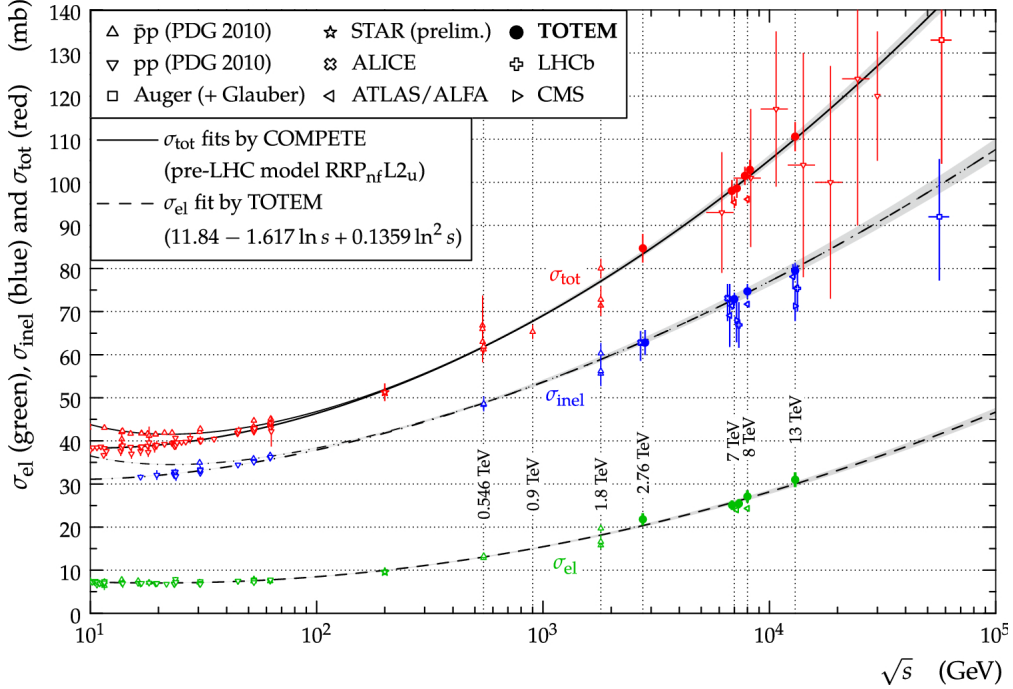
Figure 20.7: Overview of elastic ($\sigma_{\rm el}$), inelastic ($\sigma_{\rm inel}$) and total ($\sigma_{\rm tot}$) cross section data for pp and $p\bar{p}$ collisions as a function of $\sqrt{s}$. The continuous black lines (lower for pp, upper for $p\bar{p}$) represent the best fits of the total cross section data by the COMPETE collaboration [22]. The dashed line is a fit of the elastic cross section data. The dashed-dotted lines refer to the inelastic cross section and are obtained from the difference between the continuous and dashed lines. Figure from Ref. [100].

$\sigma_{\rm tot} \propto {\rm Im}[T_{\rm el}(t \to 0)]$, see Eq. (20.3). Since in practice it is not possible to measure down to $t = 0$, we need to extrapolate. To minimize the model dependence when extrapolating, it is vital to measure down to as low $|t|$ values as possible (i.e. high β^*). This method requires an independent luminosity measurement. Once the luminosity is known, $d\sigma_{\rm el}/dt$ can be normalized and used to extract $\sigma_{\rm tot}$ using the formula:

$$\sigma_{\rm tot}^2 = \frac{16\pi}{1 + \rho^2} \left.\frac{d\sigma_{\rm el}}{dt}\right|_{t \to 0} . \tag{20.44}$$

3. **Coulomb normalization.** Similarly to the previous method, this approach relies on the elastic observables only and requires a measurement of the elastic cross section at very low values of $|t|$, where it is sensitive to the theoretically well known Coulomb QED contribution $4\pi\alpha_{\rm QED}^2/t^2$. The normalization of $d\sigma_{\rm el}/dt$ is then determined by fitting the experimental data at very low $|t|$ using a formula including the Coulomb amplitude and its interference with the strongly interacting (the so-called nuclear) term. This method has been successfully used by UA4/2 [101] and TOTEM [102].

4. **Luminosity-independent.** This method does not rely on the knowledge of luminosity but rather on the knowledge of $N_{\rm el}$ and $N_{\rm inel}$ and on the optical theorem: combining equations (20.43) and (20.44) with $\frac{d\sigma_{\rm el}}{dt} = \frac{1}{\mathcal{L}}\frac{dN_{\rm el}}{dt}$ we get

$$\sigma_{\rm tot} = \frac{16\pi}{1 + \rho^2} \frac{dN_{\rm el}/dt|_{t=0}}{N_{\rm el} + N_{\rm inel}}, \tag{20.45}$$

where $\mathrm{d}N_{\mathrm{el}}/\mathrm{d}t\big|_{t=0}$ corresponds to the extrapolation to $t = 0$ of the nuclear term only. By independently and simultaneously measuring N_{el} and N_{inel}, and applying the optical theorem, we can also determine the luminosity.

The TOTEM [100, 103–105] and ATLAS [106, 107] collaborations at CERN have covered an energy range from $\sqrt{s}$=2.76 TeV to 13 TeV. A compilation of high energy total pp and $p\bar{p}$ cross section measurements is shown in Fig. 20.7 (for discussion of the pre-LHC elastic scattering data see review [108]).

Despite some tension between the Tevatron CDF [109] and E811 [110] data [12] and to a lesser extent between the TOTEM [104, 105] and ATLAS [106, 107] measurements, the data clearly indicate that in the Tevatron – LHC energy interval the total cross section starts to grow *faster* than the power-law parametrization [26] describing the data below the Tevatron energy. In particular, while the DL fit [26] predicts $\sigma_{\mathrm{tot}} = 90.7$ mb at $\sqrt{s} = 7$ TeV, the TOTEM experiment observes 98.6±2.2 mb [104].
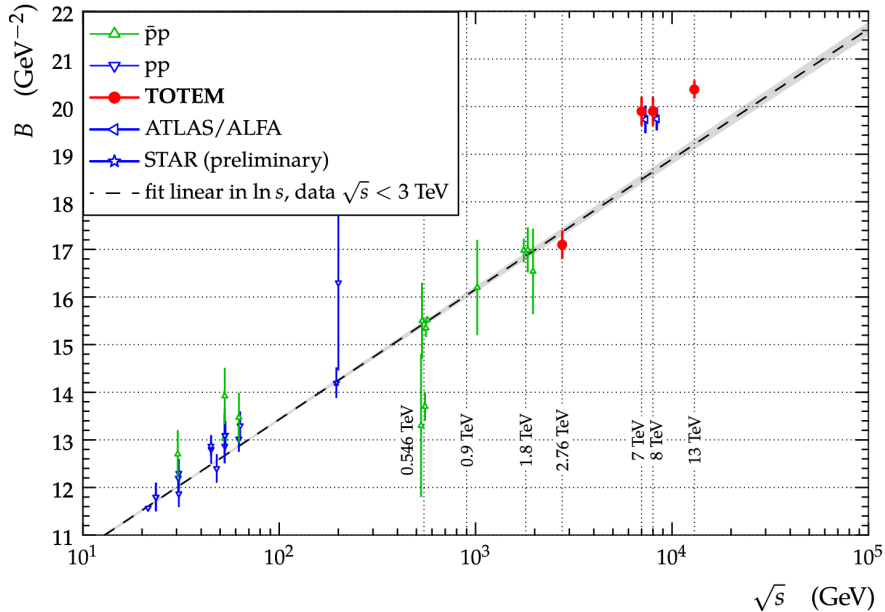

Figure 20.8: The diffractive slope B for pp and $p\bar{p}$ elastic scattering as a function of $\sqrt{s}$. The experimental uncertainties represent the quadratic sum of statistical and systematic uncertainties. The dashed line is a result of a linear fit to data at $\sqrt{s} < 3$ TeV. The data points come from [103–107, 111–113]. Figure from Ref. [100].

A compilation of the high-energy data on the elastic slope is shown in Fig. 20.8. It is clearly seen that in the TeV energy range the slope increases with $\sqrt{s}$ more rapidly than the logarithmic behaviour expected in the case of one-Pomeron exchange, see Eq. (20.30). Such an acceleration of the t-slope derivative, $\mathrm{d}B/\mathrm{d}\ln s$, is a clear manifestation of the increasing role of the multi-Pomeron exchanges, where asymptotically the slope should rise as $\ln^2 s$, see [117]. Finally, Fig. 20.9 illustrates the energy dependence of the differential elastic pp cross section. As expected (see Section 20.3.3.1), the diffractive dip moves to smaller $|t|$ with increasing energy.

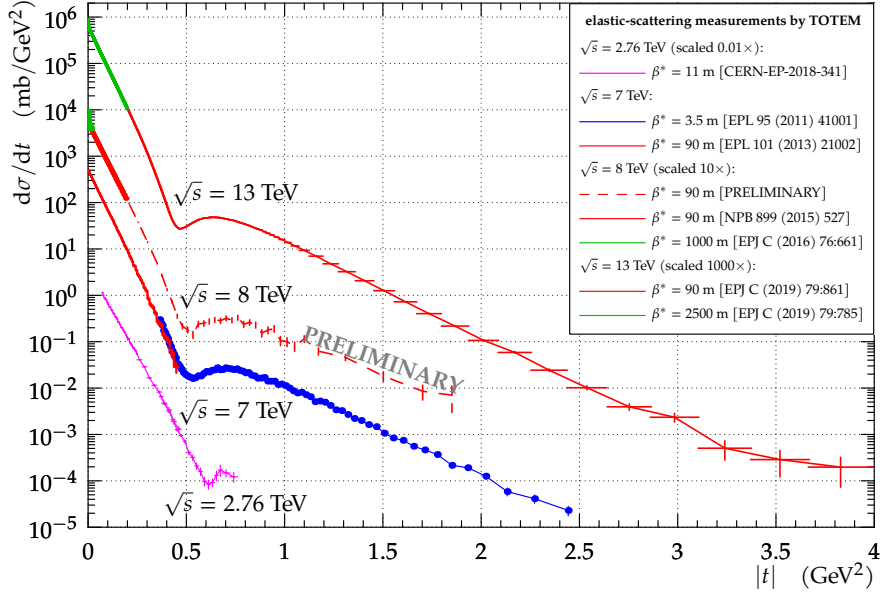[12]The CDF 1.8 TeV point [109] is 2.8 σ higher than the corresponding E811 result [110].

Figure 20.9: The t-dependence of the *pp* elastic cross section for collision energies $\sqrt{s} = 2.76$ TeV [103], 7 TeV [104, 114], 8 TeV [53, 115, 116] and 13 TeV [54, 102]. The experimental uncertainties represent the quadratic sum of statistical and systematic uncertainties. Figure from Ref. [116].

20.4.2 *Diffractive vector meson production*

The exclusive production of vector mesons was studied in detail at HERA (see for a review [91]). It is well described within the 'dipole model' (see for review and references [120]), where the incoming photon first fluctuates into a quark-antiquark, which then interacts with the target proton and, finally, with the probability given by the overlap integral between the vector meson wave function and the outgoing $q\bar{q}$-pair, the vector meson is produced. The crucial quantity is the value of cross section, $\sigma(q\bar{q} - p)$, of elastic scattering of the $q\bar{q}$-pair on the proton. The energy behaviour of $\sigma(q\bar{q} - p)$ is driven by the intercept, $\alpha_{\text{eff}}(0)$, of the effective Pomeron [13] (rightmost singularity in the *j*-plane), while the value of the cross section depends on the quark separation, *r*, in the transverse plane, $\sigma(q\bar{q} - p) \propto \alpha_s^2 \langle r^2 \rangle$ [43, 44]. Thus different processes with the same $\langle r^2 \rangle$ are driven by the same $\sigma(q\bar{q} - p)$ cross section.

In the DIS case this separation in turn is controlled by the photon virtuality, Q^2, and the quark mass, m_q: $\langle r^2 \rangle \simeq 1/(z(1-z)Q^2 + m_q^2)$ (*z* is the photon momentum fraction carried by the quark). Indeed, the cross section of the ρ meson diffractive production in DIS at $Q^2 = M_{J/\psi}^2$ is close (up to the difference in the quark electric charges) to that for the J/ψ photoproduction, see Fig. 20.10 (Left).

The production cross section depends non-trivially on W, the energy of the $\gamma^* p$ center of mass system. It increases with W as W^n, where $n = 0.2$ for ρ, ω and ϕ (light quark)-mesons but $n = 0.8$ for J/ψ. Note that in the J/ψ case the energy dependence is close to that of the BFKL (Balitsky-Fadin-Kuraev-Lipatov) Pomeron [59, 122, 123], that is, the singularity calculated within the leading (and next-to-leading) approximation in perturbative QCD. But at lower scales the absorptive (multi-Pomeron) corrections tame the growth which leads to smaller values of n ([124–127]), see Fig. 20.10 (Right).

A similar situation reveals in the dependence of α_{eff} on Q^2, as can be seen in Fig. 47 of [91]. At a large scale $\mu^2 = (Q^2 + M_V^2)/4$ the value of $\alpha_{\text{eff}} \simeq 1.3$ is close to the prediction for the QCD

---

[13]Effective Pomeron means that this is not an original pole in the *j*-plane, but it includes the corrections (renormalizations) caused by the enhanced diagrams (see e.g. [121]).
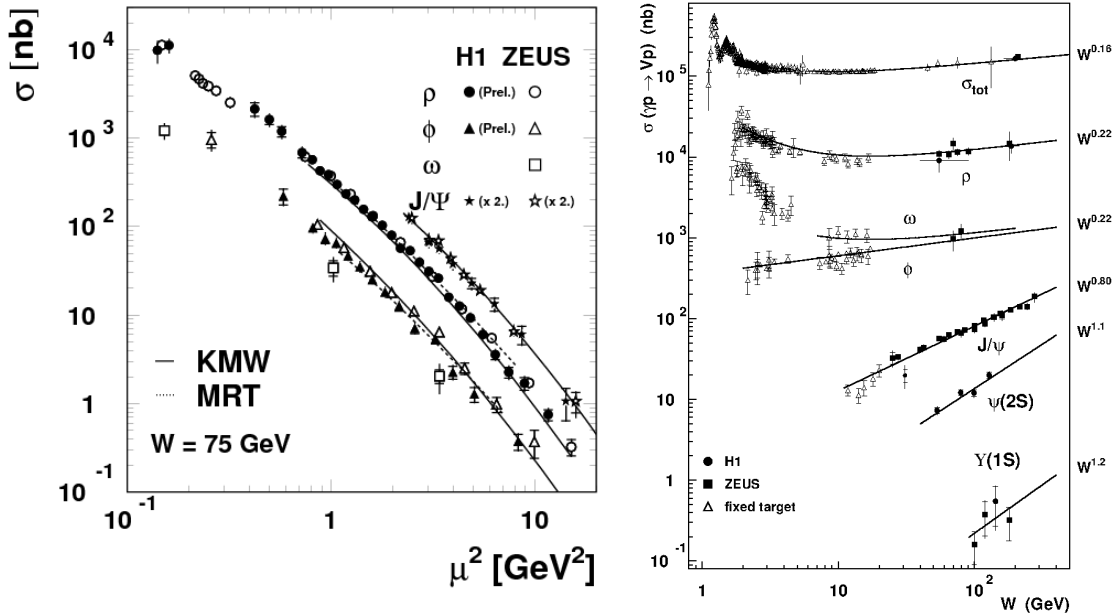
Figure 20.10: (Left) The ρ, ω, ϕ and J/ψ elastic production cross sections as a function of the scale $\mu^2 = (Q^2 + M_V^2)/4$. For readability of the figure, the J/ψ cross sections are multiplied by a factor 2. Figure from Ref. [118]. (Right) Compilation of photoproduction cross section measurements as a function of the γp centre-of-mass energy, W. The total cross section and various vector meson production cross sections are included, with the approximate power law dependences $\sigma \propto W^\delta$ indicated for each process. Figure from Ref. [119].

Pomeron, while for a smaller scale, the absorptive corrections described by the multi-Pomeron diagrams start to reduce the cross section, and α_{eff} decreases.

20.5 Pomeron in QCD

All features described in the previous Sections were based on *first principles*, such as analyticity (based on causality), unitarity, crossing symmetry, etc. Since QCD theory satisfies all these principles it should reveal a corresponding "Regge" behaviour. Indeed, within perturbative QCD there is a Pomeron: an even-signature singularity in the j-plane with vacuum quantum numbers. While in the old Regge theory the Regge trajectories and their couplings were phenomenological numbers fitted from experiment, perturbative QCD allows one to calculate the positions of the singularities and the corresponding couplings with $O(\alpha_s)$ and even with $O(\alpha_s^2)$ accuracy [59, 122, 123, 128–131].

In terms of Feynman diagrams, the QCD Pomeron may be viewed as a sum of multi-particle ladders built by the exchange of two t-channel (reggeized [14]) gluons, see the left-hand side of Fig. 20.5.

The sum of ladder diagrams of the type of Fig. 20.5 is the simplest multiparticle structure which reproduces the power-like s^α behaviour of the Pomeron pole. In other words it corresponds to a sum of completely inelastic $2 \to n$ processes, that is, to the last term $G_{\text{inel}} = 1 - \exp(-\Omega)$ in the unitarity equation (20.9). This set of diagrams was resummed in the limit of a small QCD coupling, $\alpha_s \ll 1$, but large energy, such that $\alpha_s \ln(s/s_0) \sim O(1)$ [59]. The summation results in the rightmost singularity at $j = 1 + \omega_0 > 1$. After accounting for the next-to-leading logarithmic

---
[14]That is, the virtual loop corrections to the one-gluon exchanges are included. These corrections are important in order to provide infrared stability of the results.

(NLL) corrections, the position of the singularity (Pomeron intercept) corresponds to $\omega_0 = 0.25$–0.3 depending only weakly on the scale [122, 123, 132–136], whose value is characterized by the transverse momentum, k_t, of gluons in the ladder.

It was demonstrated (see e.g. [137]) that the resummation of the $(\alpha_s \ln(1/x))^n$ terms based on the QCD Pomeron results essentially improves the description of low-x inclusive HERA data within the framework of the NNLO DGLAP evolution.

At this stage the singularity is the cut in the j-plane. However we have to account for the boundary conditions at relatively small k_t. Imposing a reasonable boundary, we arrive at a series of Regge poles in the interval from $j = 1$ to $j = 1 + \omega_0$ instead of the cut [134]. Note that the first (corresponding to the rightmost pole in the j-plane, i.e. to the pole with the largest Re j) eigenfunction consists of gluons with relatively small k_t, while for the next poles the k_t increases. DIS inclusive $\gamma^* p$ cross sections were fitted in [135] using the QCD based approach in which Pomeron is represented by series of Regge poles obtained within the perturbative QCD BFKL approach. It was concluded that the first pole has a small coupling to the proton. It is possible that this small value of the coupling to the proton is related to the fact that the enhanced multi-Pomeron diagrams (i.e. the rescattering of intermediate partons) were neglected in the fit. The main effect of this enhanced contribution is the "renormalization" of the intercept which diminishes the effective value of ω_0. Besides this, the enhanced diagrams provide a saturation by reducing the rise of the parton densities in the $(b, \; k_t, \; y)$-space (see e.g. [138, 139]).

Note that perturbative QCD allows us to understand why the values of the phenomenological multi-Pomeron vertices and the shift, ω_0, of the intercept, are small (due to $\alpha_s \ll 1$ and some numerical factors such as N_c and π). Indeed, at the lowest α_s orders we get for the ω_0 value and the simplest multi-Pomeron vertices (see e.g. [59, 139, 140]):

$$\omega_0 \propto \frac{N_c \alpha_s}{\pi}, \quad g_{3\mathbb{P}} \propto \frac{N_c \alpha_s^2}{(N_c^2 - 1)\pi^2} \quad \text{and} \quad g_2^2 \propto \frac{N_c \alpha_s}{(N_c^2 - 1)^2}, \tag{20.46}$$

where g_2^2 is the coupling corresponding to the transition of 2 into 2 Pomerons.

20.5.1　*BFKL evolution in the 'dipole' representation*

It was shown in [141–144] that the LO BFKL Pomeron equation [59] can be written in terms of the evolution of the dipole density, $N(x_d, y_d; y)$, in rapidity y (here x_d and y_d are the transverse coordinates of two t-channel gluons which form the colour singlet dipole). Indeed, after the emission of a new gluon at point z_d, the initial colour dipole with coordinates (x_d, y_d) turns into a pair of dipoles (x_d, z_d) and (z_d, y_d). This can be considered as a development of a 'dipole cascade'. Moreover in this formalism it is easy to include the non-linear absorptive corrections (last term in the square brackets in Eq. (20.47)), which accounts for the rescattering of the intermediate partons (gluons) on the target proton. The corresponding contribution is described by the so-called "fan" diagrams and these are the most important corrections to the linear DGLAP (Dokshitzer-Gribov-Lipatov-Altarelli-Parisi) evolution [145] in the case of DIS at not large scales but at very small momentum fraction [139].

The resulting non-linear evolution (Balitsky-Kovchegov equation [146–148]) reads

$$\frac{\mathrm{d}}{\mathrm{d}y} N(x_d, y_d; y) = \frac{\alpha_s N_c}{2\pi^2} \int \mathrm{d}^2 z_d \frac{(x_d - y_d)^2}{(x_d - z_d)^2 (y_d - z_d)^2}$$
$$\times \left[N(x_d, z_d; y) + N(y_d, z_d; y) - N(x_d, y_d; y) - N(x_d, z_d; y) N(y_d, z_d; y) \right]. \tag{20.47}$$

For a small density N the last term in the square brackets can be neglected, and the first three terms in Eq. (20.47) reproduce the conventional BFKL equation in the coordinate representation.

However, for large $N \to 1$ the right-hand side of Eq. (20.47) vanishes and we reach the saturation $N = 1$. It is worth mentioning that, as shown in [149], in terms of 'dipole' formalism, with the triple-Pomeron vertex generated by the 'one dipole to two dipoles' transition, it is possible to relate the Good-Walker approach to high mass diffraction with the triple-Pomeron diagram.

20.5.2 *Distribution of secondaries: theory versus experiment*

As already discussed, in terms of Feynman diagrams the cut Pomeron can be viewed as a set of ladder diagrams corresponding to a sum of completely inelastic $2 \to n$ processes, that is, to the last term $G_{\text{inel}} = 1 - \exp(-\Omega)$ in the unitarity equation (20.9). Here $n > 2$ means the production of additional $(n-2)$ gluons which, after hadronization, form minijets. [15] Therefore, in the final state driven by one Pomeron, we expect to observe gluon minijets with a flat rapidity distribution in the central (plateau) rapidity region. This would correspond to a flat pseudorapidity distribution of produced particles if they were massless. A typical pseudorapidity distribution of charged particles in inclusive events (up to $|\eta| = 7$) is shown in Fig. 20.11 (left) [150] (see also Fig. 52.1 in [1]). The central part ($|\eta| < 2.5$) was measured by CMS, while the forward region was covered by TOTEM. The dip observed at $\eta = 0$ is explained by the presence of massive particles (the Jacobian $J(p_T, m, \eta) = p_T/E \to p_T/\sqrt{p_T^2 + m^2}$ at $\eta = 0$). A photon energy spectrum is shown in Fig. 20.11 (right) [151], measured by LHCf inclusively and in events with a diffraction topology, i.e. no charged particles with $p_T > 100$ MeV and $|\eta| < 2.5$ observed by ATLAS. As expected in diffractive events the energy flow decreases with E_γ more slowly than that in the inclusive case.
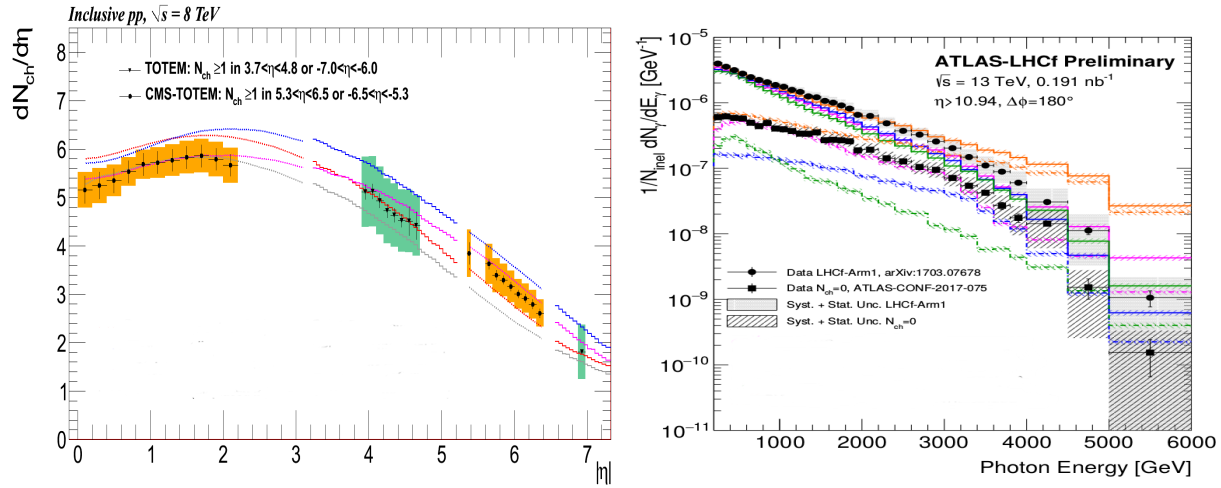

Figure 20.11: (Left) Charged-particle pseudorapidity distribution for inclusive events measured by CMS and TOTEM [150]. The error bars represent the statistical and uncorrelated systematic uncertainties between neighboring bins, while the shaded areas denote the combined statistical and full systematic uncertainties. The coloured lines indicate model predictions. (Right) Photon energy spectrum measured by LHCf at $|\eta| > 10.94$. The filled circles show the inclusive photon spectrum measured by LHCf [152] and filled squares the spectrum for $N_{\text{ch}} = 0$ events where no charged particles with $p_T > 100$ MeV and $|\eta| < 2.5$ are observed by ATLAS [153]. The coloured lines indicate model predictions. The error bars correspond to the statistical uncertainties and the shaded areas denote the combined statistical and systematic uncertainties. Figure from Ref. [151].

The energy dependence of the particle density $dN_{\text{ch}}/d\eta$ at $\eta = 0$ is shown in Fig. 20.12 (left). Neglecting absorptive corrections given by the enhanced diagrams (which mainly change ('renor-

---

[15]Minijets result from hadronization of partons emitted from the cut QCD Pomeron. Typically these are groups of hadrons with comparatively low overall $E_T \lesssim 5$–10 GeV.
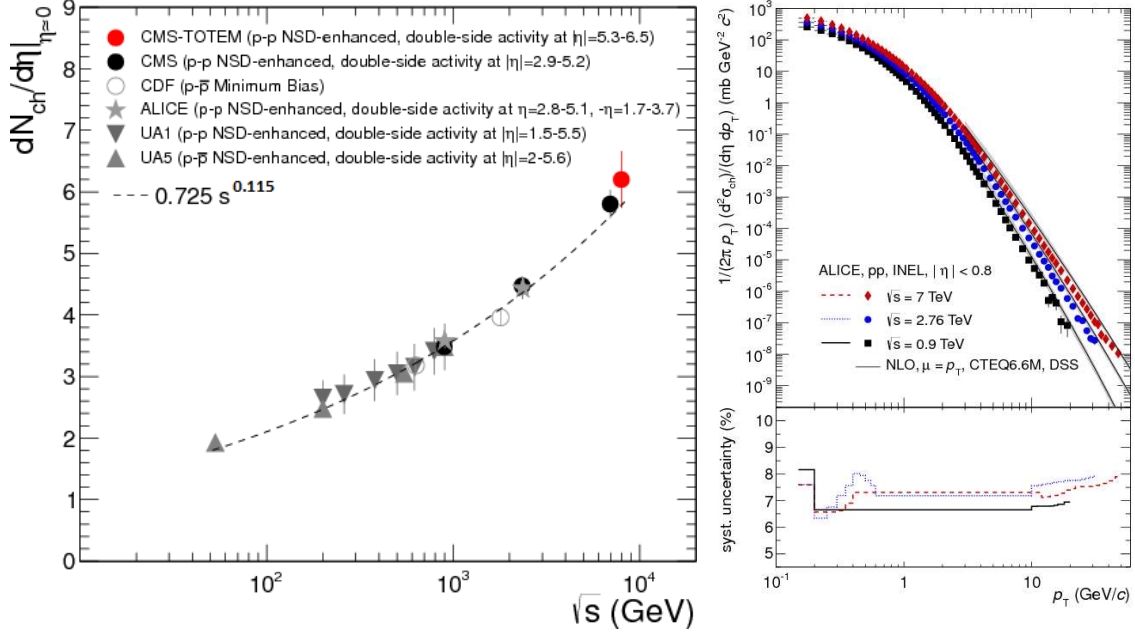
Figure 20.12: (Left) Energy dependence of the charged particle density $dN_{ch}/d\eta$ at $\eta \approx 0$ for *pp* and $p\bar{p}$ collisions. Shown are measurements performed with different Non-SD event selections from UA1 [154], UA5 [155], CDF [156,157], ALICE [158] and CMS [159]. The dashed line is a power-law fit to the data. Figure from Ref. [150]. (Right) Differential cross section of charged particles with $|\eta| < 0.8$ in inelastic *pp* collisions at $\sqrt{s} = 0.9, 2.76$ and 7 TeV as a function of p_T. Only statistical uncertainties are shown. Figure from Ref. [160].

malize') the effective Pomeron intercept $\alpha_{eff}(0) = 1 + \Delta$ [121]), we conclude that according to the AGK rules the plateau height $d\sigma/d\eta \propto s^{\Delta}$ is driven just by the one-Pomeron exchange with effective $\Delta \sim 0.2$ (see Section 20.3.3.3). That is, the density of secondaries observed in the inclusive process increases with increasing energy faster than the total cross section, whose growth is tamed by the multi-Pomeron diagrams. Indeed, as is seen from Fig. 20.12 (left), in the interval of collider energies $dN_{ch}/d\eta = (1/\sigma_{inel})d\sigma/d\eta \propto s^{0.115}$ (i.e. $d\sigma/d\eta \propto s^{0.215}$), while $\sigma_{inel} \propto s^{0.1}$.

Contrary to the 'old' Regge theory where it was *assumed* (based on the experimental data existing in the 1950s and 1960s) that all transverse momenta are limited, in QCD the k_t distributions of jets (charged particles) have a long k_t tail ($d\sigma/dk_t^2 \propto \alpha_s^2(k_t^2)/k_t^4$ at large k_t and very large energy $s \gg k_t^2$). An example of the p_T distribution of charged secondaries is shown in Fig. 20.12 (right).

Note that the mean transverse momentum of secondaries, produced via jet fragmentation, slowly increases with collision energy, see Fig. 20.13 (right). This is caused by the stronger absorption (at larger $\sqrt{s}$) of the gluons with a smaller k_t ($\sigma^{abs} \propto 1/k_t^2$). The growth of $\langle p_T \rangle$ with multiplicity (see Fig. 20.13 (left)) can be explained by the fact that events with larger N_{ch} correspond to a smaller impact parameter, b, where the absorption of a low k_t component is stronger and, next, larger multiplicity can be originated by the events with jets/minijets with higher p_T. Since the mean p_T of secondaries grows with $\sqrt{s}$, the increase with $\sqrt{s}$ of transverse energy flow is a bit faster than that of particle density.

The model [162] based on a modification of the classic RFT allows one to trace the smooth transition from the pure perturbative, large k_t, region into the *soft* domain. A strong absorption of the low k_t partons plays a crucial role here since it produces an effective infrared cutoff, k_{sat}, and provides the possibility of extending the parton approach, used for 'hard' processes, to also
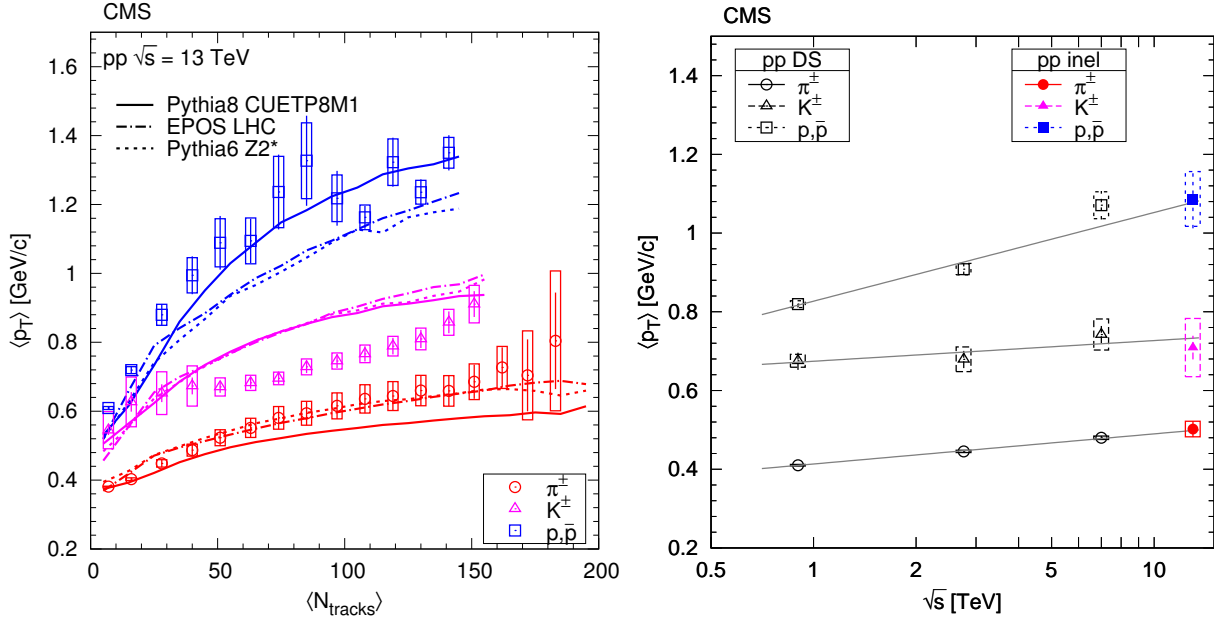
Figure 20.13: Average p_T of pions, kaons and protons in the range $|\eta| < 1.0$ as a function of (left) track multiplicity at $|\eta| < 2.4$ and (right) of center-of-mass energy where the curves show linear fits using $\ln s$. The error bars indicate the uncorrelated combined uncertainties, while the boxes show the uncorrelated systematic uncertainties. Figures from Ref. [161].

describe high-energy soft and semihard interactions. This approach combines a description of soft physics and diffraction with jet physics in a coherent self-consistent way.

Another way is to include the soft and hard components independently [37,66,163,164]. In this approach the soft part is described in terms of RFT with the phenomenological "soft" Pomeron pole while the hard part is calculated in terms of the parton model for minijet production with the energy dependent cutoff $k_t > k_0(s)$. A combined description of soft and hard processes in hadronic collisions is reached within the QGSJET Monte Carlo model (e.g. [61]) in the framework of the so-called "semi-hard Pomeron" approach (see e.g. [165]).

In [166] a model was constructed, which incorporated the attractive features of the two successful theoretical approaches to high energy QCD: BFKL Pomeron calculus [59,60] and the Colour Glass Condensate/saturation [167].

20.5.2.1 *Correlations*

All LHC experiments routinely measure tracks with $p_T > p_{\min}$, where $p_{\min}$ can vary in different studies. Typically, $p_{\min} = 200$ MeV, where tracking reconstruction efficiencies are larger than 70%. In order to identify particle species, each experiment has sophisticated identification procedures usually based on the ionization energy loss, dE/dx, or other techniques, with different regions of applicability for different particle species. Thanks to usually relatively large cross sections of soft QCD processes, most of the results below come from event samples with very low or negligible pile-up.

Following the notation in [168], symmetrized inclusive particle number densities for q points at $y_1, ..., y_q$ (where y_i represents the 4-momentum of the ith particle), $\rho_q(y_1, ..., y_q)$, are related to the inclusive differential cross section by

$$\frac{1}{\sigma_{\text{inel}}} d\sigma = \rho_1(y) dy, \quad \frac{1}{\sigma_{\text{inel}}} d^2\sigma = \rho_2(y_1, y_2) dy_1 dy_2 \quad \text{etc.} \tag{20.48}$$

By integrating we get

$$\int \rho_1(y)\mathrm{d}y = \langle n \rangle, \quad \int\int \rho_2(y_1, y_2)\mathrm{d}y_1\mathrm{d}y_2 = \langle n(n-1) \rangle \quad \text{etc.,} \tag{20.49}$$

where the angular brackets denote averaging over the event sample and n is the particle multiplicity.

Since the inclusive q-particle densities in general contain trivial contributions from lower-order densities, it is convenient to consider quantities C_q which vanish when one of their arguments becomes statistically independent of (uncorrelated with) the others. These quantities C_q, called correlation functions (or cumulant functions), are defined as:

$$C_2(1,2) = \rho_2(1,2) - \rho_1(1)\rho_1(2), \quad C_3(1,2,3) = \rho_3(1,2,3) - \sum_{(3)} \rho_1(1)\rho_2(2,3) + 2\rho_1(1)\rho_1(2)\rho_1(3),$$

$$C_4(1,2,3,4) = \rho_4(1,2,3,4) - \sum_{(4)} \rho_1(1)\rho_3(1,2,3) - \sum_{(3)} \rho_2(1,2)\rho_2(3,4) + 2\sum_{(6)} \rho_1(1)\rho_1(2)\rho_2(3,4)$$

$$- 6\rho_1(1)\rho_1(2)\rho_1(3)\rho_1(4). \tag{20.50}$$

The 2D two-particle correlation function is defined as

$$C(\Delta\eta, \Delta\phi) = \frac{\rho_2(\Delta\eta, \Delta\phi)}{\rho_1(\eta_a, \phi_a)\rho_1(\eta_b, \phi_b)}. \tag{20.51}$$

The distribution $\rho_2(\Delta\eta, \Delta\phi)$ is usually interpreted as a conditional probability to observe a particle a at the phase-space point (η_a, ϕ_a) if a particle b at (η_b, ϕ_b) is observed as well, and $\Delta\eta = \eta_a - \eta_b$ and $\Delta\phi = \phi_a - \phi_b$. The distributions $\rho_1(\eta_a, \phi_a)$ and $\rho_1(\eta_b, \phi_b)$ are probabilities to observe a single particle at (η_a, ϕ_a) and (η_b, ϕ_b), respectively. The denominator of Eq. (20.51) is constructed as a product of two single-particle distributions using an event mixing technique, where each particle in the pair comes from a different event. Experimentally, each reconstructed track is weighted by the inverse of an efficiency factor which accounts for the detector acceptance, the reconstruction and particle identification efficiencies, the contamination by secondary particles and the fraction of misreconstructed tracks.

An example of two-particle correlation functions measured in pp collisions at 7 TeV is shown in Fig. 20.14 for identical-particle pairs (right panel) and for particle–anti-particle pairs (left panel) [169].

We observe two distinct features which can be explained by short-range (in rapidity) correlations: 1) a near-side peak at $\Delta\phi \approx 0$ and 2) an away-side peak or rather a ridge at $\Delta\phi \approx \pi$. The near-side peak is considered to be caused by at least three effects:

- *fragmentation of partons scattered at a hard scale.* These relatively high p_T partons produce showers which after the hadronization form the mini-jets which create a broad structure extending over at least one unit in $\Delta\eta$ and $\Delta\phi$.

- *resonance decays.* The decay of resonances contributes to the near-side peak at $\Delta\eta \sim 0$ and extended in $\Delta\phi$ [170–172], depending on the released kinetic energy of the given resonance. This effect is mostly visible for unlike-sign particle pairs.

- *femtoscopic correlations.* The term "femtoscopic" refers to a length scale of the order of 10^{-15} m. These correlations are present at low relative momenta of the particles in a pair (representing a very small phase-space corner, so they are practically invisible in terms of $(\Delta\eta, \Delta\phi)$) and give rise to an enhancement of the correlation function (due to Bose-Einstein quantum statistics for identical bosons) or its suppression (due to Fermi-Dirac quantum statistics for
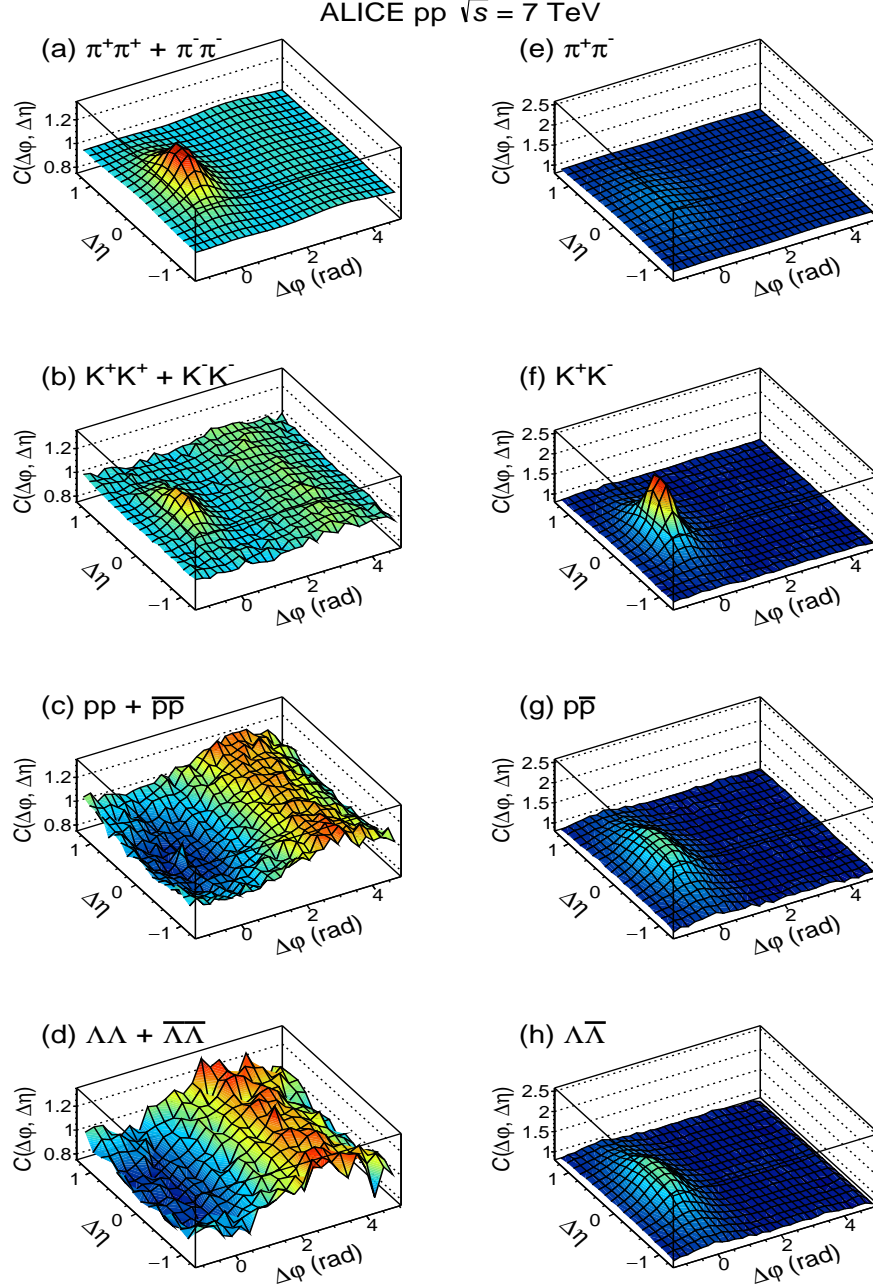
Figure 20.14: Two-particle correlation functions for identical-particle pairs: $\pi^+\pi^+ + \pi^-\pi^-$, $K^+K^+ + K^-K^-$, $pp + \bar{p}\bar{p}$, and $\Lambda\Lambda + \bar{\Lambda}\bar{\Lambda}$ (left panel) and particle–anti-particle pairs: $\pi^+\pi^-$, K^+K^-, $p\bar{p}$ and $\Lambda\bar{\Lambda}$ (right panel). Figure from Ref. [169].

identical fermions). Besides this, at low relative momenta there are correlations caused by Coulomb and/or other final state interactions. The shape of all these effects in $(\Delta\eta, \Delta\phi)$ space depend strongly on the mass of the particle type as well as on the size of the particle-emitting system. The latter is traditionally measured in Bose-Einstein correlation (BEC) analyses and is not part of this review.

The away-side peak originates from energy-momentum conservation which manifests itself by

the quark and the anti-quark going back-to-back in ϕ. In this case the rapidity width of the away-side peak is much larger than the near-side peak since in the original matrix element the quark and the antiquark can be separated by some $\Delta\eta$ interval.

As discussed in Sections 20.3.3.2 and 20.3.3.3, there may be several cut Pomerons in the same event, each giving rise to particle sets which are, in general, independent of each other (except for small Bose-Einstein correlations). This leads to long-range (in rapidity) correlations. Since the density of secondaries, dN/dy, is proportional to the number of cut Pomerons, k, the probability to observe at least one particle is proportional to $\langle k \rangle$, while the probability to observe simultaneously two particles separated by some (rather large) rapidity interval is proportional to $\langle k^2 \rangle$. Thus the long-range correlations are pedicted to be $C_2 = \langle k^2 \rangle / \langle k \rangle^2 - 1 > 0$ which depends weakly on the separation $\Delta\eta$ between the two particles [173, 174]. In the case of the pure eikonal approach, neglecting the enhanced diagrams and the conservation law effects in the proton fragmentation region, we expect that these long-range correlations,

$$C_2(\Delta y) = \frac{\sigma_{\text{inel}} d^2\sigma/dy_1 dy_2}{d\sigma/dy_1 \ d\sigma/dy_2} - 1 \sim \text{const}, \tag{20.52}$$

do not depend on the rapidity separation, $\Delta y = |y_1 - y_2|$, between the two particles. The contribution of the processes with more cut Pomerons also results in a much wider multiplicity distribution and in a larger density of soft particles coming from the 'underlying event'.
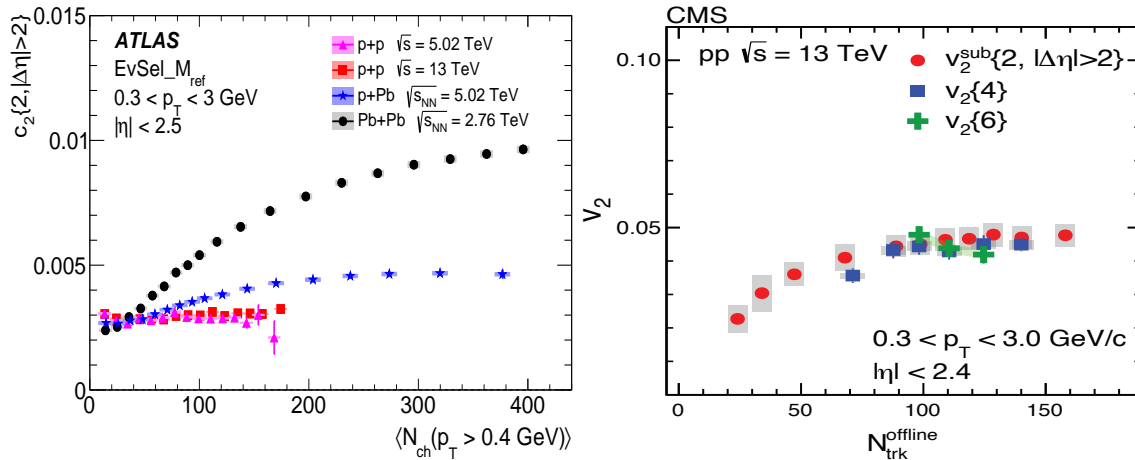

Figure 20.15: (Left) The two-particle cumulant, $c_2\{2, |\Delta\eta| > 2\}$, as a function of $\langle N_{\text{ch}}(p_T > 0.4 \text{ GeV}) \rangle$ for pp collisions at $\sqrt{s} = 5.02$ and 13 TeV, pPb collisions at $\sqrt{s_{NN}} = 5.02$ TeV and low-multiplicity $PbPb$ collisions at $\sqrt{s_{NN}} = 2.76$ TeV. The data are constructed from particles with $0.3 < p_T < 3.0$ GeV. Figure from Ref. [175]. (Right) The $v_2\{2, |\Delta\eta| > 2\}$, $v_2\{4\}$ and $v_2\{6\}$ values as a function of number of charged particles, averaged over $0.3 < p_T < 3.0$ GeV and $|\eta| < 2.4$, in pp collisions at $\sqrt{s} = 13$ TeV. Figure from Ref. [176]. The error bars correspond to the statistical uncertainties, while the shaded areas denote the systematic uncertainties.

20.5.2.2 *Color reconnection*

In this context, we have to mention also the so-called 'colour reconnection' phenomenon. This is a pure 'soft QCD' effect. The point is that after a number of coloured secondary partons are produced, there are different possibilities to form the colour flow between these partons and to group the partons into colourless clusters. In the process of reconnection, one rearranges the colour flow in such a way as to minimize the size of the clusters. This is especially important when

dealing with MPI contributions. The reconnection between the different cut Pomerons diminishes the final multiplicity and can change the form of the $N_{\rm ch}$ distributions (see e.g. Section 41.3.3 of [1] and [2, 13, 177, 178]).

20.5.2.3 *Double parton scattering*

The probability of MPI depends on the spatial distribution of partons in the incoming protons. The effects of MPI are suppressed if the density of partons is low and the partons from the incoming beam particles are separated from each other by a large interval in transverse coordinate space $\vec{x}_t$. Events in which two hard subprocesses, caused by interactions of two different parton pairs (say, $(a_1 b_1)$ and $(a_2 b_2)$), take place simultaneously, are called Double Parton Scattering (DPS). The DPS cross section is driven by the 'double parton distributions', $D(y_{a_1}, y_{a_2}, ...)$, where y_{a_1} and y_{a_2} are momentum fractions carried by the partons from the proton a and the dots denote all other coordinates. As a rule, experiments study DPS processes at relatively small momentum fractions y_i. Here, correlations due to momentum conservation (like $y_{a_1} + y_{a_2} < 1$) are not so important, and with a reasonable accuracy we can assume a factorization

$$D(y_{a_1}, y_{a_2}, ...) \propto F(y_{a_1}) \cdot F(y_{a_2}) , \tag{20.53}$$

where $F(y_{a_i})$ are the single parton distributions. In such a case the DPS cross section takes the form

$$\sigma^{\rm DPS} = c \cdot \frac{\sigma_{a_1 b_1} \sigma_{a_2 b_2}}{\sigma_{\rm eff}} , \tag{20.54}$$

where $\sigma_{a_1 b_1}$ and $\sigma_{a_2 b_2}$ are cross sections for the two *independent* hard processes, while $\sigma_{\rm eff}$ characterizes the mean area occupied by the partons a_1 and b_1; the constant factor $c = 1/2$ if both hard processes $(a_1 b_1)$ and $(a_2 b_2)$ are identical, otherwise $c = 1$. Thus the DPS cross section is sensitive to the spatial separations between partons in the proton (see Section 7.2.3 in [2] and [179, 180] for more explanations and reviews).

One problem is that within this approach we *assume* that the partons a_1 and a_2 are produced by two independent parton showers (and similarly for the other incoming proton). On the other hand, there is a probability that from the beginning we start with the evolution of a single shower which further splits into two different branches. In this case the separation between the two partons (two shower branches) becomes very small – of the order of the inverse scale ($\sim 1/\sqrt{q^2}$) at which the splitting occurs. The exact value of this 'splitting' scale q^2 depends on the particular kinematics of the DPS process. So, different experiments (with different kinematical conditions) can give somewhat different values of $\sigma_{\rm eff}$. In general, the value of $\sigma_{\rm eff}$ depends on the following features: a) on the measured process since the spatial (b_t) distributions of different incoming partons (light quarks, heavy quarks, gluons) can be different; b) on the splitting scale, $\sqrt{q^2}$, of one parton cascade into two branches. The typically high value of the splitting scale then explains the fact that the experimentally measured values of $\sigma_{\rm eff} \sim$ 7–25 mb (see Fig. 4 of [181]) are smaller than $\sigma_{\rm tot}$ or mostly even lower than the proton area $\pi R_p^2 \sim$ 22–24 mb (see e.g. [182]); c) on the p_T balance, k_T, in the individual hard process (e.g. for two dijet productions $k_T = |\overrightarrow{p_{T1}} + \overrightarrow{p_{T2}}|$ where p_{T1} and p_{T2} are jet p_T's of the first hard process (similarly for the second hard process). A small value of k_T indicates that there were no splittings or the splitting scale $\sqrt{q^2}$ was small and, therefore, we expect larger $\sigma_{\rm eff}$; d) on the contribution of single parton scatterings misidentified as DPS. For a lower scale of the hard process this contribution is larger (see [183] for more detailed discussion).

20.5.2.4 *Final state interactions*

The formalism of the RFT does not include 'final state interactions' [16]. Therefore, besides the correlations considered in the previous Section 20.5.2.1 we have to expect the correlation caused by

---

[16] In general, final state interactions can be included into the detailed structure of the multi-Pomeron vertices. However these vertices are phenomenological objects which are not well known experimentally.
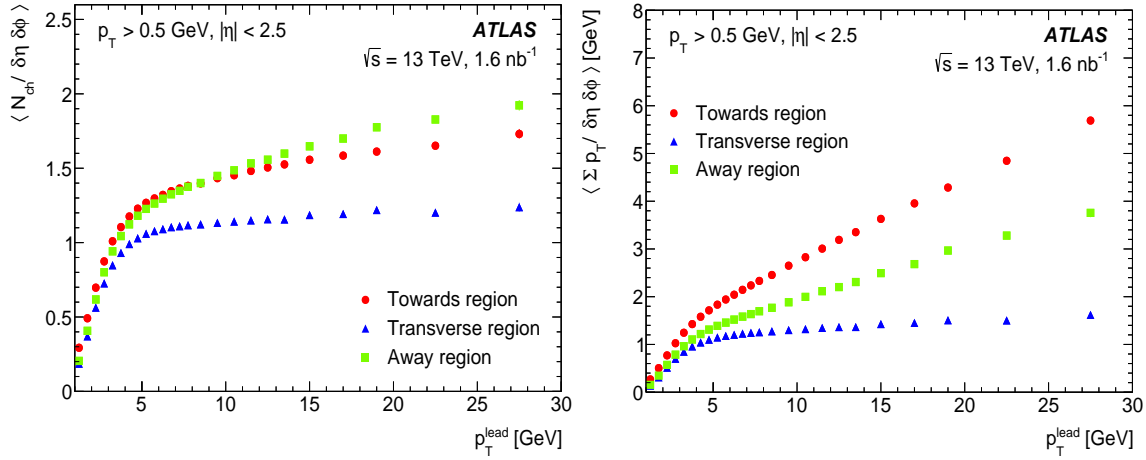
Figure 20.16: Mean charged particle density (left) and the sum of transverse momenta of secondaries (right) in events with the 'leading' high p_T particle as a function of p_T^{lead} in the transverse, towards and away azimuthal regions. Secondaries with $p_T > 0.5$ GeV and $|\eta| < 2.5$ are registered. The error bars (mostly hidden by the data markers) represent combined statistical and systematic uncertainties. Figures from [184].

partons and hadrons rescattering in the final state. These effects are not crucial at lower energies, but become more important at high LHC energies, in particular in heavy-ion collisions where the particle density is large. For example, the final state interactions (FSI) lead to the formation of the collective flow of secondaries (see e.g. [185] for a review), especially in high-multiplicity events. To study the collective flow experimentally, one has to subtract correlations coming from few-particle sources such as resonance decays, mini-jets, multi-jets and BEC (so called "non-flow"). The non-flow can efficiently be suppressed using the sub-event method, that is by studying the azimuthal correlations between particles separated in η [186], or subtracted using the multi-particle correlation (or cumulant) techniques.

The cumulant method is based on calculating $2k$-particle azimuthal correlations, $\text{corr}_n\{2k\}$, and cumulants $c_n\{2k\}$ (where $k = 1, 2, ...$), for nth Fourier harmonics. The $\text{corr}_n\{2k\}$ are defined as [187, 188]:

$$\langle\langle\text{corr}_n\{2\}\rangle\rangle = \langle\langle e^{in(\phi_1-\phi_2)}\rangle\rangle, \ \langle\langle\text{corr}_n\{4\}\rangle\rangle = \langle\langle e^{in(\phi_1+\phi_2-\phi_3-\phi_4)}\rangle\rangle,$$
$$\langle\langle\text{corr}_n\{6\}\rangle\rangle = \langle\langle e^{in(\phi_1+\phi_2+\phi_3-\phi_4-\phi_5-\phi_6)}\rangle\rangle$$

and similarly for higher numbers of correlated particles. The double-brackets $\langle\langle\rangle\rangle$ denote averaging first over particles in an event and then over events within a given event class. For every event, the average is taken over all possible combinations of azimuthal angles ϕ_l ($l = 1, ..., 2k$) of the $2k$ particles. The cumulants are then obtained from multi-particle azimuthal correlations after subtracting correlations between $2(k-1)$ particles according to the following formulae [187, 188]:

$$c_n\{2\} = \langle\langle\text{corr}_n\{2\}\rangle\rangle, \ c_n\{4\} = \langle\langle\text{corr}_n\{4\}\rangle\rangle - 2\langle\langle\text{corr}_n\{2\}\rangle\rangle^2,$$
$$c_n\{6\} = \langle\langle\text{corr}_n\{6\}\rangle\rangle - 9\langle\langle\text{corr}_n\{2\}\rangle\rangle \times \langle\langle\text{corr}_n\{4\}\rangle\rangle + 12\langle\langle\text{corr}_n\{2\}\rangle\rangle^3.$$

The cumulants for higher particle multiplicities are calculated in [187, 188]. The cumulants then serve to estimate the Fourier harmonics v_n as follows [187]:

$$v_n\{2\} = \sqrt{c_n\{2\}}, \ v_n\{4\} = \sqrt[4]{-c_n\{4\}}, \ v_n\{6\} = \sqrt[6]{c_n\{6\}/4}.$$

Some of the long-range correlation ($|\Delta\eta| > 2$) results obtained on a sample of charged particles

with $0.3 < p_T < 3.0$ GeV and $|\eta| < 2.4$ are summarized in Fig. 20.15. The left plot shows the cumulant c_2 measured for *pp*, *pPb* and *PbPb* collisions [175], while the right plot shows the elliptical harmonics v_2 measured for *pp* collisions [176], both as functions of multiplicities of charged particles. The two-particle correlations are observed to be strongest and rising with $N_{\rm ch}$ for *PbPb* collisions, and weakest and rather flat for *pp* collisions. The elliptical-flow harmonics for 4- and 6-particle correlations show again a rather flat multiplicity dependence (at least for large multiplicities). Within experimental uncertainties, the values of $v_2\{2\}, v_2\{4\}$ and $v_2\{6\}$ measured in *pp* collisions at 13 TeV are consistent with each other. The similarity between $v_2\{4\}$ and $v_2\{6\}$ suggests that some collective effects are occurring in *pp* collisions at high multiplicity and the observations are similar to those in *PbPb* collisions, where the $v_2\{4\}$ values were measured to be close to $v_2\{6\}$ but they are both lower than $v_2\{2\}$ (not shown here)).

Another example of long-range correlations is the so-called "ridge effect". Here not only the 'back-to-back' jet correlations are registered, but also an excess of particles going in the same (in the azimuthal plane) direction as the leading (relatively high p_T) hadron. Moreover, this excess is seen at the rapidities separated from the leading hadron by a rather large interval (see e.g. [189] for a review).

It is popular to describe such FSI effects within the hydrodynamic model [190], which operates with collective (thermodynamic) variables. In terms of microscopic interactions, the collective flow can be caused by the geometry of a particular collision (the absorption is smaller for the secondaries flying in the direction orthogonal to the impact parameter vector $\vec{b}$ [191, 192]), or by the colour reconnection at the hadronization stage [193], or accounting for the rescattering of secondaries directly, as was done, for example, in the AMPT model [194].

20.5.3   *The underlying event*

Except for the exclusive case, any 'hard' subprocess is accompanied by soft secondaries coming from initial state radiation (ISR), final state radiation (FSR) and multiple parton interaction (MPI), see Subsection 7.2.2 in [2]. These extra particles distort the signal we are looking for. In particular, they affect the isolation criteria applied to photons and charged leptons and the vertex reconstruction efficiency. In general, also the effects of colour reconnection (discussed in Section 20.5.2.2) contribute to the underlying event.

The usual procedure of estimating the amount of underlying event (UE) is to spatially divide tracks in each event according to their azimuthal angle into the Toward region (where the highest p_T jet points), the Away region (opposite to the Toward region) and to two Transverse regions. The standard observables are the average track multiplicity per unit area and the average scalar sum of track p_T per unit area. Figure 20.16 shows the particle density and the sum of p_T for the UE in ATLAS events containing at least one charged particle with $p_T > 0.5$ GeV and $|\eta| < 2.5$ [184].

Note that by construction the largest values of $\langle p_T \rangle$ are observed in the 'Toward' region, while in the 'Away' region we observe a slightly larger density than in the Toward region. These are results of the 'leading' and 'backward' jet fragmentation. In the transverse region, mostly filled by particles from the UE, the particle density and sum of p_T per unit $(\Delta\eta, \Delta\phi)$ area practically do not depend on the $p_T^{\rm lead}$ since these secondaries come from the other cut Pomeron(s), that is, from other 'multiple interactions'. For low $p_T^{\rm lead} < 2$ GeV the distributions in all three regions are close to each other. These events actually do not contain a 'hard' subprocess. Moreover, for a very small $p_T^{\rm lead} \to 1$ GeV we start to select soft events with abnormally low $p_T < p_T^{\rm lead}$ particles. Since only particles with $p_T > 0.5$ GeV are registered, the signal drops fast for $p_T^{\rm lead} \to 1$ GeV. As a function of collision energy $\sqrt{s}$, the energy flow in the transverse region increases as $\sum p_T \sim s^{0.2}$ (as follows from Fig. 7 (right) in [184]) due to the larger number of MPI collisions and larger $\langle p_T \rangle$
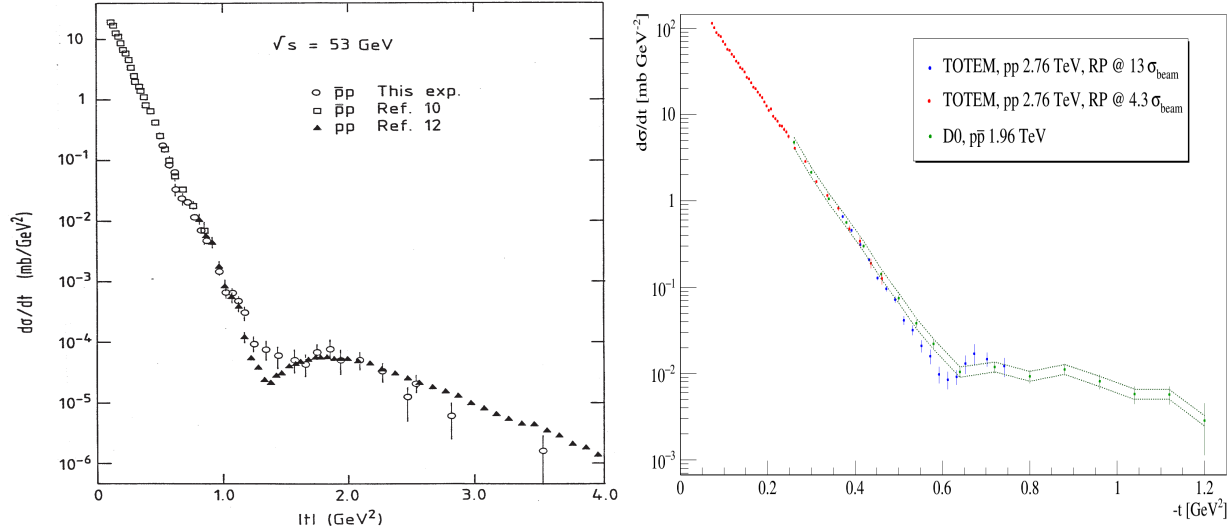
Figure 20.17: Comparison of the t-dependence of the elastic cross sections from pp and $p\bar{p}$ collisions. (Left) Data from the ISR energy of 53 GeV are shown by closed triangles [195] for pp collisions and by open circles [196] and open squares [197] for $p\bar{p}$ collisions. Only t-dependent uncertainties are shown and the systematic scale uncertainty is estimated to be $\pm 30\%$. Figure from Ref. [196]. (Right) Data from the D0 experiment at 1.96 TeV [198] are compared with data from the TOTEM experiment [103]. The green dashed line indicates the normalization uncertainty of the D0 measurement. Figure from Ref. [103].

in each collision [17]. As follows from this and other UE-dedicated LHC studies [199], from the comparisons of the data to the models with and without MPI, the necessity of MPI is convincingly demonstrated.

20.6 The Odderon

Apart from the even-signature singularity (Pomeron), in QCD with $N_c = 3$ there exists its counterpart, the odd-signature singularity placed at $j \simeq 1$ and formed by three t-channel reggeized gluons connected in colour space by the symmetric d^{abc} tensor of the colour $SU(3)$ group [200, 201]. This object is called the Odderon. The Odderon exchange amplitude has opposite sign for pp and $p\bar{p}$ scatterings. Its intercept is predicted to be very close to $j = 1$ [202–204], while according to perturbative estimates the coupling to the nucleon is rather small [205, 206]. The corresponding amplitude is mainly real and is about 100 times smaller than the imaginary part of the Pomeron exchange amplitude. Calculating the elastic amplitude via the eikonal formula (20.13) we have to replace the opacity $\Omega(b)$ by the sum $\Omega = \Omega_{\text{even}} + \Omega_{\text{odd}}$, where Ω_{even} is mainly real and Ω_{odd} is imaginary. Note that at $t = 0$ this QCD Odderon does not couple to mesons, and the t-slope of the Odderon amplitude is expected to be smaller than that for the Pomeron; instead of the singularity at $t = 4m_\pi^2$ in the Pomeron case, the nearest singularity in the Odderon channel is at $t = 9m_\pi^2$, see for instance [204]. Thus, in the impact parameter b space the QCD Odderon occupies an area of a smaller radius, see e.g. [207].

Experimentally an indication in favour of a manifestation of the high energy C-odd amplitude was observed by comparing the elastic pp and $p\bar{p}$ cross sections in the dip region (where the contribution from the C-even amplitude has a minimum) at the CERN-ISR [196], see Fig. 20.17 (left) [18].

---

[17] Recall the stronger absorption of the low k_t partons.

[18] Note that a qualitatively similar behaviour to the $p\bar{p}$ ISR data, namely a filling in of the dip in the t-distribution,

To get a better understanding of the Odderon effects it would be very instructive to have the $d\sigma_{el}/dt$ data for both pp and $p\bar{p}$ reactions at the same but higher energy ~ 1 TeV (ideally in the same apparatus) and, in the ideal case, to study the energy dependence.

At the moment we can only compare the pp cross section measured by TOTEM at $\sqrt{s} = 2.76$ TeV [103] with the $d\sigma/dt$ values measured by the D0 collaboration at 1.96 TeV in $p\bar{p}$ collisions [198], see Fig. 20.17 (right).

The situation looks quite intriguing, but needs further investigation. Note that in the TeV energy range the ω, ρ and ωP, ρP exchange contributions, which may be responsible for the difference between the pp and $p\bar{p}$ cross sections in the dip region at the ISR energies, are practically negligible.

Another way to search for the Odderon is to measure the real part of the elastic pp scattering amplitude via the interference with the pure QED one-photon exchange. Since the one-photon exchange amplitude contribution is sizeable only at very small $|t|$, this way we can study the Odderon at or near to $t = 0$. Indeed, the value of the ratio $\rho \equiv \mathrm{Re}T_{el}/\mathrm{Im}T_{el}$, obtained by TOTEM at 13 TeV ($\rho = 0.10 \pm 0.01$ [102]), turns out to be smaller than that expected for the pure even-signature amplitude, see Fig. 20.18.
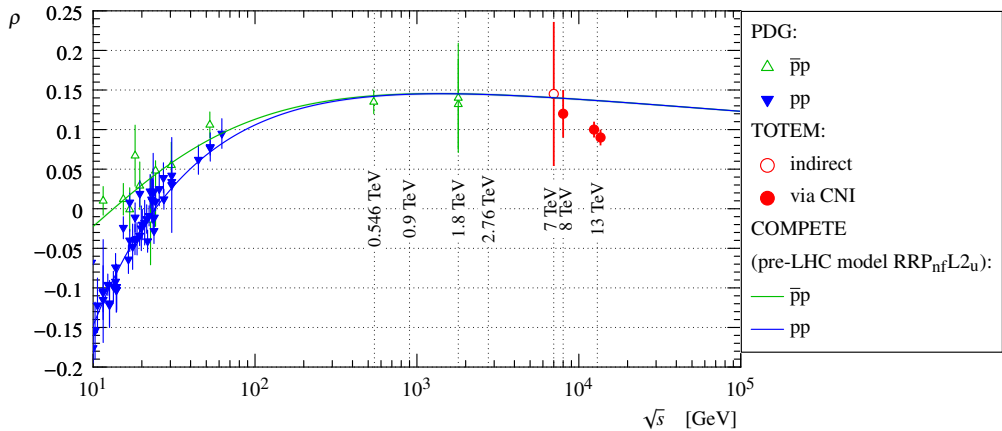

Figure 20.18: The dependence of the ρ parameter on the collision energy. The pp (blue) and $p\bar{p}$ (green) data are taken from [1]. The TOTEM measurements are marked in red. The two points at 13 TeV correspond to two fit cases, discussed in [102], using the same data. The lines represent fits to the data using the COMPETE parameterization [22]. Figure from Ref. [102].

Based on dispersion relations and assuming the C-even contribution only, from the known total cross sections we would rather expect $\rho \simeq 0.13$–0.14. The difference could indicate that the rise of the total cross section at energies above those of the LHC slows down (see the dispersion relation, Eq. (20.19)) or this could be attributed to an Odderon contribution (see e.g. [210]). However, the Odderon exchange amplitude extracted in this analysis has opposite sign to that for the lowest-α_s-order QCD Odderon, see e.g. [205, 206, 211, 212]. Besides this, the Odderon contribution to ρ, obtained in [210], grows with $\sqrt{s}$ (for $\sqrt{s} > 0.5$ TeV), while in QCD we expect that the Odderon contribution to ρ decreases with energy, since the QCD Odderon intercept is smaller than that of the QCD Pomeron.

It is worth mentioning also that the Odderon contribution is strongly screened by the multi-Pomeron diagrams, which facilitate the falling-off of ρ with energy increasing, see [213, 214]. On the other hand, analyzing the whole ensemble of high energy elastic pp ($p\bar{p}$) low $|t|$ data, a reasonable description can be obtained using the even-signature amplitude only, that is, without the Odderon.

---

was observed by the UA4 collaboration at the CERN S$p\bar{p}$S collider at $\sqrt{s}$=546 and 630 GeV(see [208, 209] and in particular Fig. 2 in [209]) and by the D0 collaboration at the Tevatron at 1.96 TeV [198].

In particular, the RR(PL2)qc model/version of the COMPETE parameterization is consistent with the TOTEM 13 TeV data on σ_{tot} and ρ within 1σ [19]. Another example is the recent analysis in [212] of the low $|t| < 0.1$ GeV^2 elastic data. Fitting all the low-t pp and $p\bar{p}$ data in the range of $\sqrt{s}$ between 13 GeV and 13 TeV without Odderon, Donnachie and Landshoff [212] succeeded to describe the TOTEM cross section with less than 1σ deviation in each $\mathrm{d}\sigma_{\text{el}}/\mathrm{d}t$ point (see Fig. 8 of [212]). Note that in this analysis, they get a larger value of ρ close to 0.14 at 13 TeV.

It was proposed also to search for the Odderon in exclusive C-even meson ($\pi^0, \eta, f_2, \eta_c, ...$) photoproduction (see e.g. [215, 216]). However the expected cross sections are small (e.g. for η_c) and in each channel there is a large background caused either by Pomeron-Pomeron fusion (such as CEP of the f_2 meson production in pp or pPb collisions) or due to the vector meson radiative decay (such as $\omega \to \pi^0\gamma$ for the case of pion) [217]. Up to now, no definitive Odderon signal in the C-even meson production has been observed. At the moment there exist only upper limits on the photoproduction cross sections obtained in the measurements at HERA at $\sqrt{s} \simeq 200$ GeV [218–220].

To conclude, let us emphasize that the existence of the C-odd singularity with intercept $\alpha_{\text{odd}}(0) \simeq 1$ is a firm prediction of QCD. At least in the high k_t region there is a well established C-odd three-gluon contribution to the scattering amplitude. However the expected coupling of such an Odderon singularity is numerically very small. Therefore it is quite challenging to observe its manifestation experimentally. Currently it seems to be a bit premature to draw any definite conclusion about an experimental observation of the Odderon signal.

20.7 Asymptotics

The high-energy behaviour of total hadronic cross sections has been one of the oldest problems of strong interactions over many decades, beginning from Heisenberg [221]. The most important bound obtained based on general analytical properties of scattering amplitudes is the FLM bound [47–49]. It states that the growth of the total hadronic cross section with energy does not exceed $\ln^2 s$, see Eq. (20.34).

Recall that we neglected the photon contribution as well as the whole electro-weak sector, and that the parameter in Eq. (20.34) s_0 is an *a priori* unknown scale. However, if we were to assume a reasonable hadronic scale, $s_0 \simeq 1\,\text{GeV}^2$, we would find that Eq. (20.34) implies an unrealistically high upper bound in comparison with the cross sections observed at present collider energies. Nevertheless there is a common trend in the literature (see for instance, reviews [222, 223] and references therein) to fit phenomenologically the total cross section with $\ln^2 s$, keeping in mind the saturation of the FLM bound. Such an asymptotic behaviour is assumed also by the COMPETE collaboration [22], which achieved a comprehensive description of all soft pre-LHC data measured at $\sqrt{s} \geq 4$ GeV as well as total pp cross sections from the LHC available in the first half of 2015 (see Section 51 in [24]).

It is interesting that the Froissart-type $\ln^2 s$ asymptotics of the pp total cross section are also supported by numerical results in lattice QCD [224]. Such a behaviour is also observed in the approach [225] based on Colour Glass Condensate saturation.

Finally, it is worth mentioning that the possibility that *asymptotically* the Pomeron intercept becomes smaller than 1, $\alpha_{\mathbb{P}}(0) < 1$, and at very high energies the total cross section starts to decrease with energy, though highly unlikely, is not yet completely rejected. For instance, such a behaviour is expected in a theory with only the triple-Pomeron coupling, $g_{3\mathbb{P}}$, and which neglects the more complicated multi-Pomeron vertices g_m^n, such as the $2 \to 2$ Pomeron coupling [226, 227].

It was also argued that in the case of an increasing (with energy) cross section the only regime consistent asymptotically with both the s- and the t-channel unitarities is that of a *black* disc whose radius increases as $R = c \cdot \ln s$ [228] (i.e. $R \propto (\ln s)^\gamma$, with $\gamma = 1$ exactly).

---

[19]We thank Jean-Rene Cudell for clarifying this issue.

20.8 Acknowledgements

References

[1] M. Tanabashi *et al.* (Particle Data Group), Phys. Rev. **D98**, 3, 030001 (2018).

[2] J. Campbell, J. Huston and F. Krauss, *The Black Book of Quantum Chromodynamics*, Oxford University Press (2017), ISBN 9780199652747, URL `https://global.oup.com/academic/product/the-black-book-of-quantum-chromodynamics-9780199652747`.

[3] R. J. Eden *et al.*, *The analytic S-matrix*, Cambridge Univ. Press, Cambridge (1966).

[4] A. Martin, Lect. Notes Phys. **3**, 1 (1969).

[5] P. D. B. Collins, *An Introduction to Regge Theory and High-Energy Physics*, Cambridge Monographs on Mathematical Physics, Cambridge Univ. Press, Cambridge, UK (2009), ISBN 9780521110358, URL `http://www-spires.fnal.gov/spires/find/books/www?cl=QC793.3.R4C695`.

[6] S. Donnachie *et al.*, Camb. Monogr. Part. Phys. Nucl. Phys. Cosmol. **19**, 1 (2002).

[7] V. N. Gribov, *The theory of complex angular momenta: Gribov lectures on theoretical physics*, Cambridge Monographs on Mathematical Physics, Cambridge University Press (2007), ISBN 9780521037037, 9780521818346, 9780511055041, URL `http://www.cambridge.org/uk/catalogue/catalogue.asp?isbn=0521307848`.

[8] S. Ostapchenko, in "25th European Cosmic Ray Symposium (ECRS 2016) Turin, Italy, September 04-09, 2016," (2016), [arXiv:1612.09461].

[9] T. Sjostrand, Int. J. Mod. Phys. **A3**, 751 (1988).

[10] B. Andersson, Camb. Monogr. Part. Phys. Nucl. Phys. Cosmol. **7**, 1 (1997).

[11] W. Kittel and E. A. De Wolf, *Soft multihadron dynamics* (2005), ISBN 9789812562951.

[12] I. M. Dremin and A. B. Kaidalov, Phys. Usp. **49**, 263 (2006), [Usp. Fiz. Nauk176,275(2006)].

[13] A. Buckley *et al.*, Phys. Rept. **504**, 145 (2011), [arXiv:1101.2599].

[14] R. Ciesielski and K. Goulianos, PoS **ICHEP2012**, 301 (2013), [arXiv:1205.1446].

[15] K. Akiba *et al.* (LHC Forward Physics Working Group), J. Phys. **G43**, 110201 (2016), [arXiv:1611.05079].

[16] G. D. Alkhazov, S. L. Belostotsky and A. A. Vorobev, Phys. Rept. **42**, 89 (1978).

[17] E. L. Feinberg and I. Y. Pomeranchuk, Doklady Akad. Nauk SSSR **93**, 439 (1953); E. L. Feinberg and I. Y. Pomeranchuk, Suppl. Nuovo Cimento **III**, serie X, 652 (1956).

[18] R. Engel, D. Heck and T. Pierog, Ann. Rev. Nucl. Part. Sci. **61**, 467 (2011).

[19] M. Gell-Mann, in "High-energy physics. Proceedings, 11th International Conference, ICHEP'62, Geneva, Switzerland, Jul 4-11, 1962," 533–542 (1962).

[20] S. Frautschi, M. Gell-Mann and F. Zachariasen, Phys. Rev. **126**, 6, 2204 (1962).

[21] K. G. Boreskov, A. B. Kaidalov and O. V. Kancheli, Phys. Atom. Nucl. **69**, 1765 (2006), [Yad. Fiz.69,1802(2006)].

[22] J. R. Cudell *et al.* (COMPETE), Phys. Rev. Lett. **89**, 201801 (2002), [hep-ph/0206172].

[23] C. Bourrely, J. Soffer and T. T. Wu, Eur. Phys. J. **C28**, 97 (2003), [hep-ph/0210264].

[24] C. Patrignani *et al.* (Particle Data Group), Chin. Phys. **C40**, 10, 100001 (2016).

[25] A. Donnachie and P. V. Landshoff, Nucl. Phys. **B231**, 189 (1984).

[26] A. Donnachie and P. V. Landshoff, Phys. Lett. **B296**, 227 (1992), [hep-ph/9209205].

[27] S. Mandelstam, Nuovo Cim. **30**, 1148 (1963).

[28] V. N. Gribov, I. Ya. Pomeranchuk and K. A. Ter-Martirosian, Phys. Lett. **9**, 269 (1964).

[29] V. A. Khoze, A. D. Martin and M. G. Ryskin, Int. J. Mod. Phys. **A30**, 08, 1542004 (2015), [arXiv:1402.2778].

[30] E. Gotsman, E. Levin and U. Maor, Int. J. Mod. Phys. **A30**, 08, 1542005 (2015), [arXiv:1403.4531].

[31] S. Ostapchenko, Phys. Rev. **D81**, 114028 (2010), [arXiv:1003.0196].

[32] V. N. Gribov, Sov. Phys. JETP **26**, 414 (1968), [Zh. Eksp. Teor. Fiz.53,654(1967)].

[33] U. Amaldi, M. Jacob and G. Matthiae, Ann. Rev. Nucl. Part. Sci. **26**, 385 (1976).

[34] A. B. Kaidalov, Phys. Rept. **50**, 157 (1979).

[35] V. Barone and E. Predazzi, *High-Energy Particle Diffraction*, volume v.565 of *Texts and Monographs in Physics*, Springer-Verlag, Berlin Heidelberg (2002), ISBN 3540421076, URL http://www-spires.fnal.gov/spires/find/books/www?cl=QC794.6.C6B37::2002.

[36] A. B. Kaidalov *et al.*, Acta Phys. Polon. **B34**, 3163 (2003), [hep-ph/0303111].

[37] L. Frankfurt and M. Strikman, in E. M. Henley and S. D. Ellis, editors, "100 Years of Subatomic Physics," 363–423 (2013), [arXiv:1304.4308].

[38] V. A. Khoze *et al.*, Eur. Phys. J. **C69**, 85 (2010), [arXiv:1005.4839].

[39] D. A. Fagundes *et al.*, Phys. Rev. **D88**, 9, 094019 (2013), [arXiv:1306.0452].

[40] R. Fiore *et al.*, Int. J. Mod. Phys. **A24**, 2551 (2009), [arXiv:0810.2902].

[41] I. M. Dremin, Phys. Usp. **56**, 3 (2013), [Usp. Fiz. Nauk 183, 3 (2013)], [arXiv:1206.5474].

[42] L. Frankfurt *et al.*, Phys. Rev. Lett. **101**, 202003 (2008), [arXiv:0808.0182].

[43] G. Bertsch *et al.*, Phys. Rev. Lett. **47**, 297 (1981).

[44] B. Z. Kopeliovich, L. I. Lapidus and A. B. Zamolodchikov, JETP Lett. **33**, 595 (1981), [Pisma Zh. Eksp. Teor. Fiz. 33, 612 (1981)].

[45] M. L. Good and W. D. Walker, Phys. Rev. **120**, 1855 (1960).

[46] J. Pumplin, Phys. Rev. **D8**, 2899 (1973).

[47] M. Froissart, Phys. Rev. **123**, 1053 (1961).

[48] A. Martin, Nuovo Cim. **A42**, 930 (1965).

[49] L. Lukaszuk and A. Martin, Nuovo Cim. **A52**, 122 (1967).

[50] A. A. Anselm and V. N. Gribov, Phys. Lett. **40B**, 487 (1972).

[51] G. Cohen-Tannoudji, V. V. Ilyin and L. L. Jenkovszky, Lett. Nuovo Cim. **5S2**, 957 (1972), [Lett. Nuovo Cim.5,957(1972)].

[52] V. A. Khoze, A. D. Martin and M. G. Ryskin, Eur. Phys. J. **C18**, 167 (2000), [hep-ph/0007359].

[53] G. Antchev *et al.* (TOTEM), Nucl. Phys. **B899**, 527 (2015), [arXiv:1503.08111].

[54] G. Antchev *et al.* (TOTEM), Eur. Phys. J. **C79**, 10, 861 (2019), [arXiv:1812.08283].

[55] L. Caneschi and A. Pignotti, Phys. Rev. Lett. **22**, 1219 (1969).

[56] O. V. Kancheli, JETP Lett. **11**, 267 (1970), [Pisma Zh. Eksp. Teor. Fiz. 11, 397 (1970)].

[57] A. H. Mueller, Phys. Rev. **D4**, 150 (1971).

[58] D. Amati, A. Stanghellini and S. Fubini, Nuovo Cim. **26**, 896 (1962).

[59] V. S. Fadin, E. A. Kuraev and L. N. Lipatov, Phys. Lett. **60B**, 50 (1975); E. A. Kuraev, L. N. Lipatov and V. S. Fadin, Sov. Phys. JETP **44**, 443 (1976), [Zh. Eksp. Teor. Fiz.71,840(1976)]; E. A. Kuraev, L. N. Lipatov and V. S. Fadin, Sov. Phys. JETP **45**, 199 (1977), [Zh. Eksp. Teor. Fiz.72,377(1977)]; I. I. Balitsky and L. N. Lipatov, Sov. J. Nucl. Phys. **28**, 822 (1978), [Yad. Fiz.28,1597(1978)].

[60] B. L. Ioffe, V. S. Fadin and L. N. Lipatov, *Quantum chromodynamics: Perturbative and nonperturbative aspects*, volume 30, Cambridge Univ. Press (2010), ISBN 9781107424753, 9780521631488, 9780511717444, URL http://www.cambridge.org/de/knowledge/isbn/item2710695.

[61] S. Ostapchenko, Phys. Rev. **D83**, 014018 (2011), [arXiv:1010.1869].

[62] J. L. Cardy, Nucl. Phys. **B75**, 413 (1974).

[63] A. B. Kaidalov *et al.*, Phys. Lett. **45B**, 493 (1973).

[64] E. G. S. Luna *et al.*, Eur. Phys. J. **C59**, 1 (2009), [arXiv:0807.4115].

[65] T. Sjöstrand, Adv. Ser. Direct. High Energy Phys. **29**, 191 (2018), [arXiv:1706.02166].

[66] K. Werner, F.-M. Liu and T. Pierog, Phys. Rev. **C74**, 044902 (2006), [hep-ph/0506232].

[67] V. A. Abramovsky, V. N. Gribov and O. V. Kancheli, Yad. Fiz. **18**, 595 (1973), [Sov. J. Nucl. Phys. 18, 308 (1974)].

[68] G. Alberi and G. Goggi, Phys. Rept. **74**, 1 (1981).

[69] K. A. Goulianos, Phys. Rept. **101**, 169 (1983).

[70] D. Bernard *et al.* (UA4), Phys. Lett. **B186**, 227 (1987).

[71] R. E. Ansorge *et al.* (UA5), Z. Phys. **C33**, 175 (1986).

[72] N. A. Amos *et al.* (E710), Phys. Lett. **B301**, 313 (1993).

[73] F. Abe *et al.* (CDF), Phys. Rev. **D50**, 5535 (1994).

[74] G. Aad *et al.* (ATLAS), Eur. Phys. J. **C72**, 1926 (2012), [arXiv:1201.2808].

[75] V. Khachatryan *et al.* (CMS), Phys. Rev. **D92**, 1, 012003 (2015), [arXiv:1503.08689].

[76] B. Abelev *et al.* (ALICE), Eur. Phys. J. **C73**, 6, 2456 (2013), [arXiv:1208.4968].

[77] G. Aad *et al.* (ATLAS), Phys. Lett. **B754**, 214 (2016), [arXiv:1511.00502].

[78] G. Aad *et al.* (ATLAS), JHEP **02**, 042 (2020), [arXiv:1911.00453].

[79] A. M. Sirunyan *et al.* (CMS and TOTEM) (2020), [arXiv:2002.12146].

[80] V. A. Khoze, A. D. Martin and M. G. Ryskin, Eur. Phys. J. **C73**, 2503 (2013), [arXiv:1306.2149].

[81] V. A. Khoze, A. D. Martin and M. G. Ryskin, Eur. Phys. J. **C23**, 311 (2002), [hep-ph/0111078].

[82] M. G. Albrow, T. D. Coughlin and J. R. Forshaw, Prog. Part. Nucl. Phys. **65**, 149 (2010), [arXiv:1006.1289].

[83] M. Albrow, Int. J. Mod. Phys. **A29**, 1402006 (2014).

[84] H. G. Fischer, W. Geist and M. Makariev, Int. J. Mod. Phys. **A29**, 28, 1446005 (2014).

[85] A. Kirk, Int. J. Mod. Phys. **A29**, 28, 1446001 (2014), [arXiv:1408.1196].

[86] M. A. Reyes *et al.* (E690), Phys. Rev. Lett. **81**, 4079 (1998).

[87] G. Gutierrez and M. A. Reyes, Int. J. Mod. Phys. **A29**, 28, 1446008 (2014), [arXiv:1409.8243].

[88] Y. L. Dokshitzer, D. Diakonov and S. I. Troian, Phys. Rept. **58**, 269 (1980).

[89] M. Derrick *et al.* (ZEUS), Phys. Lett. **B315**, 481 (1993).

[90] T. Ahmed *et al.* (H1), Nucl. Phys. **B429**, 477 (1994).

[91] P. Newman and M. Wing, Rev. Mod. Phys. **86**, 3, 1037 (2014), [arXiv:1308.3368].

[92] A. Aktas *et al.* (H1), Eur. Phys. J. **C48**, 715 (2006), [hep-ex/0606004].

[93] S. Chekanov *et al.* (ZEUS), Nucl. Phys. **B816**, 1 (2009), [arXiv:0812.2003].

[94] F. D. Aaron *et al.* (H1), Eur. Phys. J. **C72**, 2074 (2012), [arXiv:1203.4495].

[95] F. D. Aaron *et al.* (H1, ZEUS), Eur. Phys. J. **C72**, 2175 (2012), [arXiv:1207.4864].

[96] A. Aktas *et al.* (H1), JHEP **10**, 042 (2007), [arXiv:0708.3217].

[97] A. Aktas *et al.* (H1), Eur. Phys. J. **C50**, 1 (2007), [hep-ex/0610076].

[98] S. Chekanov *et al.* (ZEUS), Nucl. Phys. **B672**, 3 (2003), [hep-ex/0307068].

[99] E. G. de Oliveira, A. D. Martin and M. G. Ryskin, Phys. Lett. **B695**, 162 (2011), [arXiv:1010.1366].

[100] G. Antchev *et al.* (TOTEM), Eur. Phys. J. **C79**, 2, 103 (2019), [arXiv:1712.06153].

[101] C. Augier *et al.* (UA4/2), Phys. Lett. **B316**, 448 (1993).

[102] G. Antchev *et al.* (TOTEM), Eur. Phys. J. **C79**, 9, 785 (2019), [arXiv:1812.04732].

[103] G. Antchev *et al.* (TOTEM), Eur. Phys. J. **C80**, 2, 91 (2020), [arXiv:1812.08610].

[104] G. Antchev *et al.* (TOTEM), EPL **101**, 2, 21002 (2013).

[105] G. Antchev *et al.* (TOTEM), Phys. Rev. Lett. **111**, 1, 012001 (2013).

[106] G. Aad *et al.* (ATLAS), Nucl. Phys. **B889**, 486 (2014), [arXiv:1408.5778].

[107] M. Aaboud *et al.* (ATLAS), Phys. Lett. **B761**, 158 (2016), [arXiv:1607.06605].

[108] M. M. Block and R. N. Cahn, Rev. Mod. Phys. **57**, 563 (1985).

[109] F. Abe *et al.* (CDF), Phys. Rev. **D50**, 5550 (1994).

[110] C. Avila *et al.* (E811), Phys. Lett. **B445**, 419 (1999).

[111] W. Guryn, "Invited talk at the Workshop on Diffraction and Low-x Physics, Reggio Calabria, Italy, August 26th–September 1st, 2018," .

[112] K. Nakamura *et al.* (Particle Data Group), J. Phys. **G37**, 075021 (2010).

[113] F. J. Nemes, PoS **DIS2017**, 059 (2018).

[114] G. Antchev *et al.* (TOTEM), EPL **95**, 4, 41001 (2011), [arXiv:1110.1385].

[115] G. Antchev *et al.* (TOTEM), Eur. Phys. J. **C76**, 12, 661 (2016), [arXiv:1610.00603].

[116] J. Kaspar, "Invited talk at the meeting of the LHC Working Group on Forward Physics and Diffraction, CERN, Switzerland, December 16-17th, 2019," .

[117] V. A. Schegelsky and M. G. Ryskin, Phys. Rev. **D85**, 094024 (2012), [arXiv:1112.3243].

[118] A. Bruni, X. Janssen and P. Marage, in "Proceedings, HERA and the LHC Workshop Series on the implications of HERA for LHC physics: 2006-2008," 427–439 (2008), [arXiv:0812.0539].

[119] A. Levy, in "Proceedings, 17th International Workshop on Deep-Inelastic Scattering and Related Subjects (DIS 2009): Madrid, Spain, April 26-30, 2009," 177 (2009), [arXiv:0907.2178].

[120] J. R. Forshaw, R. Sandapen and G. Shaw, JHEP **11**, 025 (2006), [hep-ph/0608161].

[121] A. Capella *et al.*, Nucl. Phys. **B593**, 336 (2001), [hep-ph/0005049].

[122] V. S. Fadin and L. N. Lipatov, Phys. Lett. **B429**, 127 (1998), [hep-ph/9802290].

[123] M. Ciafaloni and G. Camici, Phys. Lett. **B430**, 349 (1998), [hep-ph/9803389].

[124] F. D. Aaron *et al.* (H1), JHEP **05**, 032 (2010), [arXiv:0910.5831].

[125] C. Adloff *et al.* (H1), Eur. Phys. J. **C13**, 371 (2000), [hep-ex/9902019].

[126] J. Breitweg *et al.* (ZEUS), Eur. Phys. J. **C6**, 603 (1999), [hep-ex/9808020].

[127] S. Chekanov *et al.* (ZEUS), PMC Phys. **A1**, 6 (2007), [arXiv:0708.1478].

[128] M. Ciafaloni, Nucl. Phys. **B296**, 49 (1988).

[129] S. Catani, F. Fiorani and G. Marchesini, Phys. Lett. **B234**, 339 (1990).

[130] S. Catani, F. Fiorani and G. Marchesini, Nucl. Phys. **B336**, 18 (1990).

[131] G. Marchesini, Nucl. Phys. **B445**, 49 (1995), [hep-ph/9412327].

[132] G. P. Salam, JHEP **07**, 019 (1998), [hep-ph/9806482].

[133] M. Ciafaloni and D. Colferai, Phys. Lett. **B452**, 372 (1999), [hep-ph/9812366].

[134] H. Kowalski, L. N. Lipatov and D. A. Ross, Eur. Phys. J. **C76**, 1, 23 (2016), [arXiv:1508.05744].

[135] H. Kowalski *et al.*, Eur. Phys. J. **C77**, 11, 777 (2017), [arXiv:1707.01460].

[136] S. J. Brodsky *et al.*, JETP Lett. **70**, 155 (1999), [hep-ph/9901229].

[137] R. D. Ball *et al.*, Eur. Phys. J. **C78**, 4, 321 (2018), [arXiv:1710.05935].

[138] E. M. Levin and M. G. Ryskin, Phys. Rept. **189**, 267 (1990).

[139] L. V. Gribov, E. M. Levin and M. G. Ryskin, Phys. Rept. **100**, 1 (1983).

[140] E. M. Levin, M. G. Ryskin and A. G. Shuvaev, Nucl. Phys. **B387**, 589 (1992).

[141] A. H. Mueller, Phys. Rept. **73**, 237 (1981).

[142] A. H. Mueller, Nucl. Phys. **B415**, 373 (1994).

[143] A. H. Mueller and B. Patel, Nucl. Phys. **B425**, 471 (1994), [hep-ph/9403256].

[144] N. N. Nikolaev, B. G. Zakharov and V. R. Zoller, JETP Lett. **59**, 6 (1994), [hep-ph/9312268].

[145] V. N. Gribov and L. N. Lipatov, Sov. J. Nucl. Phys. **15**, 438 (1972), [Yad. Fiz.15,781(1972)]; G. Altarelli and G. Parisi, Nucl. Phys. **B126**, 298 (1977); Y. L. Dokshitzer, Sov. Phys. JETP **46**, 641 (1977), [Zh. Eksp. Teor. Fiz. 73, 1216 (1977)].

[146] I. Balitsky, Nucl. Phys. **B463**, 99 (1996), [hep-ph/9509348].

[147] I. Balitsky, Phys. Rev. **D60**, 014020 (1999), [hep-ph/9812311].

[148] Y. V. Kovchegov, Phys. Rev. **D60**, 034008 (1999), [hep-ph/9901281].

[149] G. Gustafson, Phys. Lett. **B718**, 1054 (2013), [arXiv:1206.1733].

[150] S. Chatrchyan *et al.* (CMS, TOTEM), Eur. Phys. J. **C74**, 10, 3053 (2014), [arXiv:1405.0722].

[151] Q.-D. Zhou (LHCF, ATLAS), EPJ Web Conf. **208**, 05008 (2019).

[152] O. Adriani *et al.* (LHCf), Phys. Lett. **B780**, 233 (2018), [arXiv:1703.07678].

[153] M. Aaboud *et al.* (ATLAS) , ATLAS-CONF-2017-075.

[154] C. Albajar *et al.* (UA1), Nucl. Phys. **B335**, 261 (1990).

[155] G. J. Alner *et al.* (UA5), Z. Phys. **C33**, 1 (1986).

[156] T. Aaltonen *et al.* (CDF), Phys. Rev. **D79**, 112005 (2009), [Erratum: Phys. Rev.D82,119903(2010)], [arXiv:0904.1098].

[157] F. Abe *et al.* (CDF), Phys. Rev. **D41**, 2330 (1990), [,119(1989)].

[158] K. Aamodt *et al.* (ALICE), Eur. Phys. J. **C68**, 89 (2010), [arXiv:1004.3034].

[159] V. Khachatryan *et al.* (CMS), Phys. Rev. Lett. **105**, 022002 (2010), [arXiv:1005.3299].

[160] B. B. Abelev *et al.* (ALICE), Eur. Phys. J. **C73**, 12, 2662 (2013), [arXiv:1307.1093].

[161] A. M. Sirunyan *et al.* (CMS), Phys. Rev. **D96**, 11, 112003 (2017), [arXiv:1706.10194].

[162] M. G. Ryskin, A. D. Martin and V. A. Khoze, Eur. Phys. J. **C71**, 1617 (2011), [arXiv:1102.2844].

[163] X.-N. Wang, Phys. Rept. **280**, 287 (1997), [hep-ph/9605214].

[164] S. Ostapchenko and M. Bleicher, Universe **5**, 5, 106 (2019).

[165] F. M. Liu *et al.*, J. Phys. **G28**, 2597 (2002), [hep-ph/0109104].

[166] E. Gotsman, E. Levin and U. Maor, Acta Phys. Polon. Supp. **8**, 777 (2015).

[167] Y. V. Kovchegov and E. Levin, Camb. Monogr. Part. Phys. Nucl. Phys. Cosmol. **33**, 1 (2012).

[168] E. A. De Wolf, I. M. Dremin and W. Kittel, Phys. Rept. **270**, 1 (1996), [hep-ph/9508325].

[169] J. Adam *et al.* (ALICE), Eur. Phys. J. **C77**, 8, 569 (2017), [arXiv:1612.08975].

[170] V. Khachatryan *et al.* (CMS), JHEP **09**, 091 (2010), [arXiv:1009.4122].

[171] K. Eggert *et al.*, Nucl. Phys. **B86**, 201 (1975).

[172] B. Alver *et al.* (PHOBOS), Phys. Rev. **C75**, 054913 (2007), [arXiv:0704.0966].

[173] E. M. Levin and M. G. Ryskin, Sov. J. Nucl. Phys. **20**, 280 (1975), [Yad. Fiz.20,519(1974)].

[174] A. Capella and A. Krzywicki, Phys. Rev. **D18**, 4120 (1978).

[175] M. Aaboud *et al.* (ATLAS), Eur. Phys. J. **C77**, 6, 428 (2017), [arXiv:1705.04176].

[176] V. Khachatryan *et al.* (CMS), Phys. Lett. **B765**, 193 (2017), [arXiv:1606.06198].

[177] S. Gieseke, "Invited talk at the Workshop on Multiple Partonic Interactions at the LHC, Prague, Czech Republic, November 18th–26th, 2019," .

[178] S. Kundu, B. Mohanty and D. Mallick (2019), [arXiv:1912.05176].

[179] M. Diehl, D. Ostermeier and A. Schafer, JHEP **03**, 089 (2012), [Erratum: JHEP03,001(2016)], [arXiv:1111.0910].

[180] T. Sjostrand and P. Z. Skands, JHEP **03**, 053 (2004), [hep-ph/0402078].

[181] M. Aaboud *et al.* (ATLAS), Phys. Lett. **B790**, 595 (2019), [Phys. Lett.790,595(2019)], [arXiv:1811.11094].

[182] M. G. Ryskin and A. M. Snigirev, Phys. Rev. **D83**, 114047 (2011), [arXiv:1103.3495].

[183] B. Blok *et al.*, Eur. Phys. J. **C74**, 2926 (2014), [arXiv:1306.3763].

[184] M. Aaboud *et al.* (ATLAS), JHEP **03**, 157 (2017), [arXiv:1701.05390].

[185] R. Snellings, New J. Phys. **13**, 055008 (2011), [arXiv:1102.3010].

[186] M. Aaboud *et al.* (ATLAS), Phys. Rev. **C97**, 2, 024904 (2018), [arXiv:1708.03559].

[187] N. Borghini, P. M. Dinh and J.-Y. Ollitrault, Phys. Rev. **C63**, 054906 (2001), [arXiv:nucl-th/0007063].

[188] A. Bilandzic, R. Snellings and S. Voloshin, Phys. Rev. **C83**, 044913 (2011), [arXiv:1010.0233].

[189] W. Li, Mod. Phys. Lett. **A27**, 1230018 (2012), [arXiv:1206.0148].

[190] B. Schenke, J. Phys. **G38**, 124009 (2011), [arXiv:1106.6012].

[191] K. G. Boreskov, A. B. Kaidalov and O. V. Kancheli, Eur. Phys. J. **C58**, 445 (2008), [arXiv:0809.0625].

[192] K. G. Boreskov, A. B. Kaidalov and O. V. Kancheli, Phys. Atom. Nucl. **72**, 361 (2009), [Yad. Fiz.72,390(2009)].

[193] C. Bierlich and J. R. Christiansen, Phys. Rev. **D92**, 9, 094010 (2015), [arXiv:1507.02091].

[194] Z.-W. Lin *et al.*, Phys. Rev. **C72**, 064901 (2005), [arXiv:nucl-th/0411110].

[195] E. Nagy *et al.*, Nucl. Phys. **B150**, 221 (1979).

[196] A. Breakstone *et al.*, Phys. Rev. Lett. **54**, 2180 (1985).

[197] A. Breakstone *et al.* (AMES-BOLOGNA-CERN-DORTMUND-HEIDELBERG-WARSAW), Nucl. Phys. **B248**, 253 (1984).

[198] V. M. Abazov *et al.* (D0), Phys. Rev. **D86**, 012009 (2012), [arXiv:1206.0687].

[199] V. Khachatryan *et al.* (CMS) , CMS-PAS-FSQ-16-008.

[200] J. Bartels, Nucl. Phys. **B175**, 365 (1980).

[201] J. Kwiecinski and M. Praszalowicz, Phys. Lett. **94B**, 413 (1980).

[202] M. A. Braun (1998), [hep-ph/9805394].

[203] J. Bartels, L. N. Lipatov and G. P. Vacca, Phys. Lett. **B477**, 178 (2000), [hep-ph/9912423].

[204] C. Ewerz (2003), [hep-ph/0306137].

[205] M. Fukugita and J. Kwiecinski, Phys. Lett. **83B**, 119 (1979), [,625(1979)].

[206] M. G. Ryskin, Sov. J. Nucl. Phys. **46**, 337 (1987), [Yad. Fiz.46,611(1987)].

[207] J. Bartels, C. Contreras and G. P. Vacca (2019), [arXiv:1910.04588].

[208] M. Bozzo *et al.* (UA4), Phys. Lett. **155B**, 197 (1985).

[209] D. Bernard *et al.* (UA4), Phys. Lett. **B171**, 142 (1986).

[210] E. Martynov and B. Nicolescu, Eur. Phys. J. **C79**, 6, 461 (2019), [arXiv:1808.08580].

[211] A. Donnachie and P. V. Landshoff, Phys. Lett. **123B**, 345 (1983).

[212] A. Donnachie and P. V. Landshoff, Phys. Lett. **B798**, 135008 (2019), [arXiv:1904.11218].

[213] J. Finkelstein *et al.*, Phys. Lett. **B232**, 257 (1989).

[214] V. A. Khoze, A. D. Martin and M. G. Ryskin, Phys. Lett. **B780**, 352 (2018), [arXiv:1801.07065].

[215] W. Kilian and O. Nachtmann, Eur. Phys. J. **C5**, 317 (1998), [hep-ph/9712371].

[216] J. Bartels *et al.*, Eur. Phys. J. **C20**, 323 (2001), [hep-ph/0102221].

[217] L. A. Harland-Lang *et al.*, Phys. Rev. **D99**, 3, 034011 (2019), [arXiv:1811.12705].

[218] J. Olsson (H1), in "New trends in high-energy physics: Experiment, phenomenology, theory. Proceedings, International Conference, Yalta, Crimea, Ukraine, September 22-29, 2001," 79–87 (2001), [hep-ex/0112012].

[219] C. Adloff *et al.* (H1), Phys. Lett. **B544**, 35 (2002), [hep-ex/0206073].

[220] T. Berndt (H1), Acta Phys. Polon. **B33**, 3499 (2002), [,182(2002)].

[221] W. Heisenberg, Z. Phys. **133**, 65 (1952).

[222] G. Pancheri and Y. N. Srivastava, Eur. Phys. J. **C77**, 3, 150 (2017), [arXiv:1610.10038].

[223] M. M. Block, Phys. Rept. **436**, 71 (2006), [hep-ph/0606215].

[224] M. Giordano, E. Meggiolaro and N. Moretti, JHEP **09**, 031 (2012), [arXiv:1203.0961].

[225] E. Ferreiro *et al.*, Nucl. Phys. **A710**, 373 (2002), [hep-ph/0206241].

[226] P. Grassberger and K. Sundermeyer, Phys. Lett. **77B**, 220 (1978).

[227] K. G. Boreskov, in M. Olshanetsky and A. Vainshtein, editors, "Multiple facets of quantization and supersymmetry," 322–351 (2001), [hep-ph/0112325].

[228] V. A. Khoze, A. D. Martin and M. G. Ryskin, Phys. Lett. **B787**, 167 (2018), [arXiv:1809.10406].